Investigation of the Aerodynamic and Acoustic Performance of a Scaled eVTOL Propeller in Axial and Non-Axial Flight

Ryan D. Lundquist

Thesis submitted to the Faculty of the
Virginia Polytechnic Institute and State University
in partial fulfillment of the requirements for the degree of

Master of Science
in
Aerospace Engineering

W. Nathan Alexander, Chair
Nanyaporn Intaratep
William J. Devenport

February 7, 2025
Blacksburg, Virginia

Keywords: Urban Air Mobility, Electric Vertical Takeoff and Landing, Propeller Aerodynamics, Propeller Acoustics

Investigation of the Aerodynamic and Acoustic Performance of a Scaled eVTOL Propeller in Axial and Non-Axial Flight

Ryan D. Lundquist

(ABSTRACT)

With the recent emergence of Urban Air Mobility (UAM) as a potential solution to alleviate congested urban transportation, concerns have arisen regarding adherence to noise emission regulations and general public acceptance. With the design of new and innovative air vehicles utilizing electric Vertical Takeoff and Landing (eVTOL) propulsion systems for UAM applications, significant gaps remain in the understanding of their aerodynamic and acoustic performance, particularly when interacting with disturbances such as turbulence generated by buildings. To address safety, noise, and performance challenges, effective optimization methods must be developed. However, there is a lack of sufficient experimental data to support these advancements. This study investigates the aerodynamic and acoustic performance of a scaled eVTOL propeller operating in both axial and non-axial flight. A comprehensive summary of the experimental propeller's design is provided. Thrust, torque, and sound pressure data are acquired from wind tunnel testing of the experimental propeller operating with various blade pitch angles, yaw angles, and under several inflow velocities. The experimental results are subsequently compared to a custom-developed Blade Element Momentum Theory (BEMT) utility for low-fidelity predictions. The findings aim to provide baseline data for Computational Fluid Dynamic (CFD) validation, enhancing predictive tools for advancing safe and efficient urban air transportation. Experimental results exhibit positive correlations between thrust, torque, and acoustic intensity with increasing yaw angle. The acoustic profile of the propeller at large yaw angles features an increase in broadband noise, a characteristic feature of Blade-Wake Interaction. Additionally, BEMT calculations predict thrust and torque within 10% accuracy of the measured data across most conditions. Supplementary calculations of the induced velocity fields offer preliminary insights into the distortion effects for future studies on interactions between eVTOL propellers and turbulent flows.

Investigation of the Aerodynamic and Acoustic Performance of a Scaled eVTOL Propeller in Axial and Non-Axial Flight

Ryan D. Lundquist

(GENERAL AUDIENCE ABSTRACT)

Urban Air Mobility (UAM) is viewed as a solution to congested transportation in urban areas. Newly designed aircraft, essentially ”air taxis”, seek to provide transportation in and around urban landscapes. A great concern with the operation of UAM aircraft in densely populated environments is their noise emissions. Methods must be developed to optimize vehicle performance while balancing the goal of being quiet enough for public acceptance. However, there remain knowledge gaps about how these vehicles will perform in such environments where turbulent flows are common. Therefore, experimental data must be acquired to provide a better understanding of how to model their performance and interactions. This study presents a comprehensive overview of the design and wind tunnel experimentation of a scaled air taxi propeller. Experimental results on aerodynamic and acoustic performance are collected and analyzed to provide baseline data for the validation of computational methods. Experimental results show trends of increasing thrust, torque, and acoustic intensity with increasing propeller tilt angle. The acoustic profile of the propeller at large tilt angles features an increase in broadband noise, which is characteristic of an increased presence of unsteady interaction. Lastly, low-fidelity calculations accurately predict thrust and torque within 10% error of the measured data for most conditions.

Dedication

To my parents, sister, Mimi and Pop Pop, Grandma, my late grandfather, and the rest of my family—your unwavering love, support, and encouragement have been the foundation of all my efforts and achievements. To my friends, who have always stood by my side, offering advice, motivation, and, most importantly, laughter during challenging times. You have all been my strength, joy, and inspiration during this journey of mine.

Acknowledgments

First and foremost, I would like to express my deepest gratitude to my advisor, Dr. Nathan Alexander, for providing me with this invaluable opportunity and for your unwavering guidance throughout my graduate career. Your mentorship and insightful feedback have played a crucial role in my academic growth and have profoundly shaped my work. To my committee members, Dr. Intaratep and Dr. Davenport, thank you for your continued support and crucial insights that have contributed to my work.

I would also like to thank Dr. Sheryl Grace and the NASA ULI team for not only providing the opportunity to undertake this research but also for cultivating an environment of collaboration and learning. To my research partners—Steve Huang, Shreyas Chaware, and ThanhLong (T-Dog) Duong—thank you for your consistent advice, mentorship, and camaraderie since my first day as a graduate student. The moments of collaboration with all of you have been where I've learned the most.

I am also deeply grateful to Joby Aviation, for their collaboration in this research and for providing me with an amazing work experience as a summer intern. The support, mentorship, and encouragement I received during my time at Joby emphasized the importance and appreciation of my research efforts. To my fellow interns at Joby, thank you for your friendship and for the lasting memories we've created together.

Lastly, I want to give my sincerest thanks to the Center for Research and Engineering in Aero/Hydrodynamic Technologies (CREATe) and its members for fostering a community of support and resources that have been vital to my efforts. A special thank you to Sherry Gong for help in navigating the often hectic logistics and many purchase orders involved in experimental research. To my office mates and fellow researchers—Charlie Gallucio, Charlie Van Horn, Muhammad Raza, and Kevin Fernandez— thank you for your constant support, more than occasional jokes, and for answering my seemingly endless and stupid questions.

Thank you all so much,
Ryan

Contents

List of Figures

List of Tables

List of Abbreviations

Abbreviations

BAI	blade-airframe interaction
BEMT	Blade Element Momentum Theory
BPF	blade passage frequency
BVI	blade-vortex interaction
BWI	blade-wake interaction
eVTOL	electric vertical take-off and landing
FWI	fuselage-wake interaction
NASA	National Aeronautics and Space Administration
PALM	parallelized large-eddy simulation model
SPL	sound pressure level
SWT	Stability Wind Tunnel
TIN	turbulence ingestion noise
UAM	urban air mobility
VTSWT	Virginia Tech Stability Wind Tunnel

Nomenclature

α	local angle of attack, deg
$\dot{m}$	mass flow rate, kg/s
Ω	angular velocity, RPM
ω	angular velocity, rad/s
ϕ	inflow angle, deg
ϕ_{ob}	observer horizontal bearing angle, deg
Ψ	yaw angle, deg

ψ	azimuth angle, deg
ρ	density, kg/m^3
σ	blade solidity
θ	sectional pitch angle, deg
θ_{ob}	observer vertical elevation angle, deg
A'	tangential force per unit length, N/m
a'	tangential induction factor
a	axial induction factor
A_2	area upstream propeller disk, m^2
A_3	area downstream propeller disk, m^2
A_∞	freestream area, m^2
A_d	propeller disk area, m^2
A_w	downstream wake area, m^2
B	number of blades
c	local chord length, m/s
C_D	drag force coefficient
C_L	lift force coefficient
C_n	normal force coefficient
C_P	power coefficient
C_Q	torque coefficient
C_T	thrust coefficient
C_t	tangential force coefficient
F	Prandtl tip loss correction factor
f	local Prandtl tip loss correction factor
N'	normal force per unit length, N/m

p_2	pressure upstream propeller disk, Pa
p_3	pressure downstream propeller disk, Pa
p_∞	freestream pressure, Pa
p_w	pressure in downstream wake, Pa
Q'	torque per unit length, Nm/m
R	blade radius, m/s
r	local radial length, m/s
r_{ob}	observer distance, m
T'	thrust per unit length, N/m
U_∞	freestream velocity, m/s
U_l	local velocity, m/s
U_n	normal velocity, m/s
U_p	in-plane velocity, m/s
U_t	tangential velocity, m/s
U_{tip}	tip velocity, m/s
V_2	velocity upstream propeller disk, m/s
V_3	velocity downstream propeller disk, m/s
V_∞	freestream velocity, m/s
V_d	velocity across propeller disk, m/s
V_w	velocity in downstream wake, m/s
V_{tip}	tip velocity, m/s

Chapter 1

Introduction

1.1 Motivation

Urban Air Mobility (UAM) has recently garnered significant interest as a potential solution to the challenges of urban transportation. UAM technologies offer efficient and safe aerial transit, seeking to connect urban centers and mitigate congestion in high-density populations. However, with the recent emergence of UAM, concerns regarding noise pollution have arisen. Given that the industry's success is heavily contingent on public acceptance and maintaining acceptable noise levels, there has been an increasing desire to expand knowledge of UAM aerodynamic and acoustic performance while operating in urban environments [26].

Unlike conventional aircraft, UAM vehicles are expected to operate in densely populated regions. Typically designed with electric Vertical Take-Off and Landing (eVTOL) capabilities, these vehicles will likely utilize vertiports located in proximity to or atop buildings. As UAM vehicles navigate through the ”urban canyon”, they will inevitably encounter complex flows and fluctuating wind conditions, which can significantly influence both noise generation and overall performance. A similar flow environment has been investigated through a Large-eddy Simulation of an urban neighborhood located in Boston, shown in Figure 1.1. This simulation, performed using the PArallelized Large-Eddy Simulation Model (PALM), depicts the flow patterns around buildings for a relatively calm day, with a freestream velocity of 3.5 m/s [1]. This clearly illustrates that as a UAM vehicle navigates through such an environment, turbulent wakes produced by buildings will introduce side wind and upwash variations onto the vehicle, reducing its overall performance. Disturbances of a much larger scale, significantly exceeding the chord length of a UAM vehicle, are of even greater interest due to the amplified disruption of aerodynamic performance and control. Vehicle trim adjustments will thus be necessary when encountering large-scale disturbances, creating a challenge in balancing the optimization of flight performance and noise reduction.

A preliminary investigation carried out by NASA regarding UAM suggests gaps exist in the understanding of vehicle performance and acoustics. NASA highlights inadequacies relating to the availability of tools and databases for use in the advancement of UAM technologies, further summarized in Rizzi et al..UAM vehicle design is trending towards utilizing multiple small propellers operating at lower tip mach numbers, resulting in lower noise profiles when compared to conventional aircraft. However, initial investigations of multi-propeller concepts have omitted to study geometries representative of future operating UAM aircraft, including propeller geometry and varying flight configurations (Figure 1.2), and have lacked critical experimental data, particularly regarding broadband noise measurements [26]. In order to achieve acceptable uncertainty in noise prediction methods and trim state optimization tools, new techniques must be developed. However, the development of predictive tools for UAM applications is hindered by the limited availability of experimental data that can be leveraged in the validation of such tools [19].

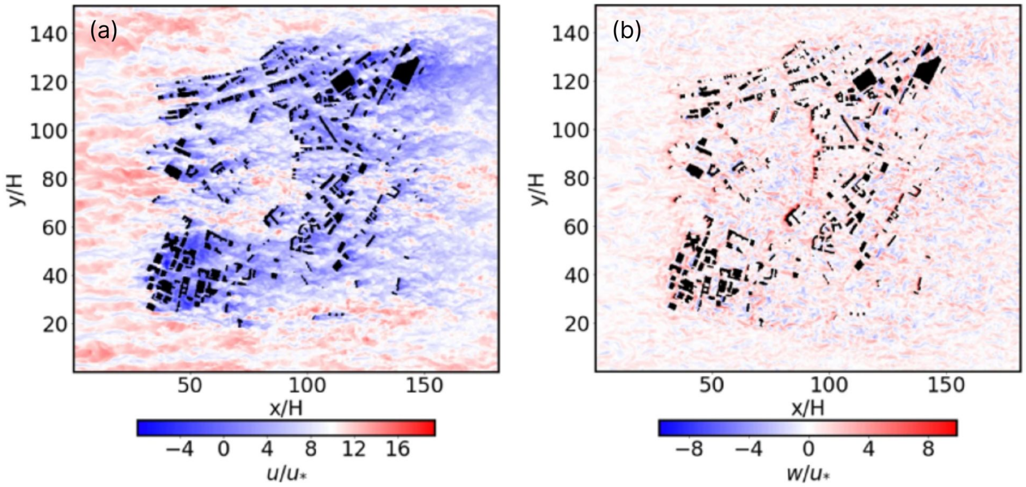

Figure 1.1: Horizontal slice of the instantaneous snapshot for **a.** streamwise velocity at z/H = 1 and **b.** vertical velocity at z/H = 1. Streamwise and vertical velocity are normalized by the friction velocity u_* (Adapted from Akinlabi et al.)

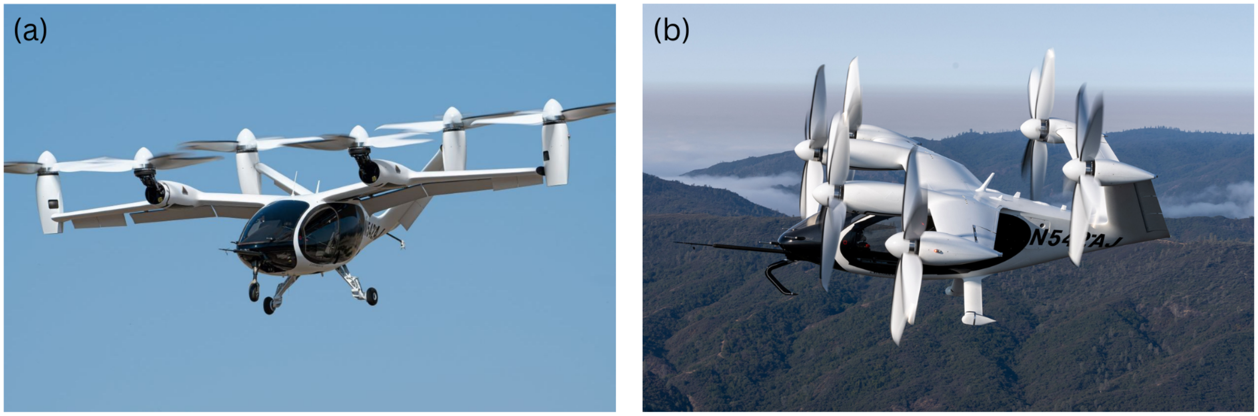

Figure 1.2: Full-scale preproduction prototype of Joby Aviation's eVTOL UAM vehicle operating in **a.** thrustborne (edgewise) flight and **b.** wingborne (axial) flight (Adapted from Thai et al.)

1.2 Research Objectives

This paper discusses a portion of a larger research initiative. The overarching objective of this initiative is to develop computational methods for predicting noise and the performance of multi-propeller concepts operating in realistic urban flow conditions. These methods will be validated through experimental testing and aid in bridging a gap in knowledge that is critical in enabling the safe and optimal operation of Urban Air Mobilities in urban settings. This research is structured around investigating the effect of urban flows and vehicle trim states on UAM performance and noise generation as a metric for flight path planning. In investigating this topic of interest, a series of comprehensive experiments are planned to study multi-propeller UAM concepts in varying flow conditions and trim states. These experiments will be employed in the validation of computational methods developed primarily by Boston University, Embry Riddle Aeronautical University, and Tuskegee University. The tasks of Virginia Tech have been systematically divided into four experimental studies:

1. Study of performance and noise characteristics of a single propeller at various loading conditions.
2. Study of performance and noise characteristics of a single propeller subjected to transient disturbances
3. Study of performance and noise characteristics of a multi-propeller configuration at various trim conditions
4. Study of performance and noise characteristics of a multi-propeller configuration subjected to transient disturbances

The content presented in this paper focuses on accomplishing the first experimental study listed above. In order to achieve a better understanding of multi-propeller concepts' performance, a baseline study must first be conducted to investigate the performance of a single propeller configuration operating at various loading conditions. Therefore, the objectives of this study are as follows:

- Design and fabricate a scaled UAM propeller for application in wind tunnel experimentation
- Evaluate baseline aerodynamic and acoustic performance of a scaled UAM propeller for computational validation in axial and non-axial flight
- Apply Blade Element Momentum Theory (BEMT) to develop a utility for validating experimental propeller performance and enabling prediction of propeller performance parameters in axial and non-axial flight

Chapter 2

Background and Literature Review

2.1 Urban Air Mobility Propeller Design

The recent emergence of UAM as a potential solution to urban transportation has resulted in the development of various design solutions. Estimated to carry a maximum of 6 passengers for no longer than 100 nautical miles with flight speeds of 200 knots or less and payload between 800 to 8000 pounds, it is the market consensus for UAM to utilize eVTOL capabilities Rizzi et al.. An eVTOL's fully electric or hybrid electric propulsion allows for the distribution of multiple smaller propulsion systems operating at lower tip speeds. eVTOL designs consist of many concepts including, but not limited to, "vector thrust", "lift + cruise", and "wingless" configurations. Vectored thrust designs use wings for cruise flight and a single distributed propulsion system for both hover and cruise. Lift+cruise designs include the use of wings for cruise, but utilize separate propulsion systems for hover and cruise operations. Lastly, wingless eVTOLs consist of multi-propeller designs without wings, capable of efficient hover flight, but limited in cruise. Analysis by Bacchini and Cestino indicates that vectored thrust designs offer optimal performance for long-range urban transportation while still offering comparable performance at short and mid-ranges. Current wingless design concepts are unable to complete long-range missions while lift-cruise designs are nearing their limit due to parasitic drag from the inoperable propellers during cruise flight.

Given the favorability of vectored thrust concepts for urban transportation, propeller designs must balance the performance demands of both cruise and hover flight while also adhering to noise emission acceptance criteria. Rizzi et al. suggests increasing the number of blades, optimizing the geometry of the airfoil, and reducing the rotation speed to optimize the propeller design within aerodynamic and acoustic constraints. Since wings generate the majority of lift during cruise flight, the thrust required from each propeller is only a fraction of what is needed in hover. As a result, the thrust requirement for hover becomes the primary design constraint [29]. Distributed propellers are optimally designed with 3-6 blades to meet hover thrust requirements while allowing for lower rotational speeds to reduce noise [10, 20]. Propeller design optimization has been conducted using Blade Element Momentum Theory and CFD solvers, incorporating constraints for both hover and cruise flight. The results indicate that non-linear distributions of chord, twist, and thickness effectively minimize power losses caused by compressibility effects at the propeller tip during cruise flight [7, 10, 24]. Further analysis of optimal blade design carried out by Shahjahan et al. includes the transition phase in the criteria. This optimization led to a noticeable reduction in chord length compared to propellers designed without accounting for transition. Conversely, transition-optimized propellers featured overall increased pitch angles. This adjustment is necessary to mitigate blade stall on the retreating blade during the transition phase [24]. While blade geometry optimization has been investigated rigorously for aerodynamic and acoustic performance of isolated propellers, gaps remain in the potential to leverage certain design aspects, such as irregular blade spacing and variable blade length. Additionally, the optimization of multi-propeller configurations and trim states is constrained by the limited availability of experimental data for CFD validation. Concepts regarding optimal propeller spacing, phasing, and active control have been explored to a limited extent [23]. The contents of this paper seek to provide baseline experimental data for an isolated propeller with future applications to optimize propeller trim in the presence of propeller-propeller and propeller-environment interactions.

2.2 Blade Element Momentum Theory

2.2.1 Overview

The Blade Element Momentum Theory (BEMT) model uses propeller geometry and characteristics of the interacting freestream flow to evaluate and predict the production of thrust and torque of a propeller system. BEMT combines Blade Element Theory and Momentum Theory to relate local spanwise blade element interactions to the macroscopic momentum transfer through the propeller plane. Blade Element Theory, first introduced by William Froude [21], is based on discretizing the blade into sections, or blade elements, and expressing the loads as functions of an element's cross-sectional geometry and local flow characteristics. The loads are expressed by experimentally derived coefficients of lift and thrust, which relate the forces on a blade cross-section to the angle between the blade and the flow, i.e. the angle of attack. The differential forces are then integrated along the blade span to achieve global values [14].

The Momentum Theory, also known as the Actuator Disk Theory, was introduced by William J. M. Rankine, where in contrast to Blade Element Theory, the propeller's blade geometry is disregarded and is rather modeled in its entirety by a pressure jump, represented by an infinitely thin actuator disk enclosed in a streamtube. Momentum Theory thus assumes the propeller to be “infinite-bladed”, rotating with infinite speed, which imparts a uniform acceleration of the fluid resulting in uniformly distributed thrust [13]. Initially only considering the axial component of induction by the propeller, the Momentum Theory was modified and refined by Hermann Glauert, who crucially introduced the rotational component of the fluid induced by the propeller [9].

BEMT couples these two theories together by discretizing the Momentum Theory streamtube into N annular rings, corresponding to N differential blade elements along the blade span defined by Blade Element Theory. These annular rings act independently from each other. The derivation of BEMT begins by applying the Momentum Theory upon a control volume as illustrated in Figure 2.1 labeled as CV_1. Three regions are defined in the control volume: the far-field, the propeller disk, and the propeller wake, denoted by the subscripts ∞, d, and w respectively. Applying the conservation of mass for these regions yields Equation 2.1.

$$\rho V_\infty A_\infty = \rho V_d A_d = \rho V_d A_d = \rho V_w A_w \tag{2.1}$$

Now applying the conservation of linear momentum to the far-field and wake components and subsequently equating to the thrust of the propeller, assuming the pressure in the control volume returns to the atmospheric pressure, resulting in no pressure change:

$$\rho V_\infty(-V_\infty A_\infty) + \rho V_d(V_d A_d) = T' \tag{2.2}$$

Equation 2.1 and Equation 2.2 are then combined to give a relation for thrust:

$$T' = \rho V_d A_d(V_w - V_\infty) = \dot{m}(V_w - V_\infty) \tag{2.3}$$

Note that the derived thrust is per unit length, due to the fact we are considering each differential annular disk. A linear momentum balance is then applied for a control volume just upstream and downstream of the propeller disk, CV_2, where $A_2 = A_3 = A_d$ and $V_2 = V_3 = V_d$. This results in Equation 2.4, which includes the pressure change imparted by the propeller.

$$\begin{gathered} \rho V_2(-V_2 A_2) + \rho V_3(V_3 A_3) = T' + p_2 A_2 - p_3 A_3 \\ T' = (p_3 - p_2) A_d \end{gathered} \tag{2.4}$$

Equating the derived relationships for thrust together and simplifying yields:

$$\rho V_d(V_w - V_\infty) = (p_3 - p_2) \tag{2.5}$$

Applying Bernoulli's equation upstream and downstream of the propeller to relate the jump in pressure to the velocity components, then subtracting Equation 2.6 from Equation 2.7 results in the relation shown in Equation 2.8.

$$p_\infty + \frac{1}{2}\rho V_\infty^2 = p_2 + \frac{1}{2}\rho V_2^2 \tag{2.6}$$

$$p_3 + \frac{1}{2}\rho V_3^2 = p_w + \frac{1}{2}\rho V_w^2 \tag{2.7}$$

$$p_3 - p_2 = \frac{1}{2}\rho(V_w^2 - V_\infty^2) \tag{2.8}$$

Substituting Equation 2.8 back into Equation 2.5 and simplifying to achieve a relation between the velocity components:

$$V_d = \frac{1}{2}(V_w + V_\infty) \tag{2.9}$$

Thus, we can define the velocity components in terms of the freestream velocity component plus some additional induced velocity normalized by V_∞, called the axial induction factor a.

$$V_d = V_\infty(1 + a) \tag{2.10}$$

$$V_w = V_\infty(1 + 2a) \tag{2.11}$$

Thrust can now be described using Equation 2.12.

$$T' = 4\pi r \rho V_\infty^2 (1 + a)a \tag{2.12}$$

To include the rotational velocity components, we consider the angular momentum for time-invariant forces, following similar step results in the relationship for the angular velocities at the propeller disk and the far-field where a' is the tangential induction factor. This results in the following equation for torque per unit length:

$$Q' = 4\pi r^3 \rho V_\infty \omega (1 + a)a' \tag{2.13}$$

Thrust and torque can also be defined by the geometric aerodynamics described by Blade Element Theory. For a given blade section, representative of an airfoil, the local velocity components and forces are detailed in Figure 2.2, where the normal and tangential components are:

$$U_n = V_\infty(1 + a) \tag{2.14}$$

$$U_t = \omega r(1 - a') \tag{2.15}$$

Geometric relationships for the local angle of attack α, sectional pitch θ_p, inflow angle ϕ, and relative local velocity U_l are defined as:

$$\alpha = \theta_p - \phi \tag{2.16}$$

$$\phi = \arctan(\frac{U_n}{U_t}) \tag{2.17}$$

$$U_l = \sqrt{U_n^2 + U_t^2} \tag{2.18}$$

Coefficients of the normal and tangential forces are related to the local lift and drag coefficients through the following rotation matrix

$$\begin{bmatrix} C_n \\ C_t \end{bmatrix} = \begin{bmatrix} \cos\phi & -\sin\phi] \\ \sin\phi & cos\phi \end{bmatrix} \begin{bmatrix} C_l \\ C_d \end{bmatrix} \tag{2.19}$$

where the local lift and drag coefficients can be determined through analytical, computational, or experimental methods. The normal and tangential forces can then be found using their respective coefficients, and subsequently used to solve for the thrust and torque per unit length, where c is the section chord length and B is the number of blades.

$$N' = C_n \frac{1}{2} \rho U_l^2 c \tag{2.20}$$

$$T' = N'B \tag{2.21}$$

$$A' = C_t \frac{1}{2} \rho U_l^2 c \tag{2.22}$$

$$Q' = A'rB \tag{2.23}$$

Equating the results for thrust and torque from both Momentum Theory and Blade Element Theory provides an implicit relation for the axial and tangential induction factors:

$$a = \frac{1}{\frac{4\sin\phi^2}{\sigma C_n} - 1} \tag{2.24}$$

$$a' = \frac{1}{\frac{4\sin\phi\cos\phi}{\sigma C_t} + 1} \tag{2.25}$$

Where the local blade solidity, σ, is defined as the ratio of the area of the propeller blades to the area of the propeller disk:

$$\sigma = \frac{Bc}{2\pi r} \tag{2.26}$$

Despite forming explicit solutions for the axial and tangential induction factors, these expressions rely on information regarding the flow angle and airfoil geometry. No closed-form solution exists, therefore an iterative solution is typically used to approximate the induction factors for a finite blade section [17].

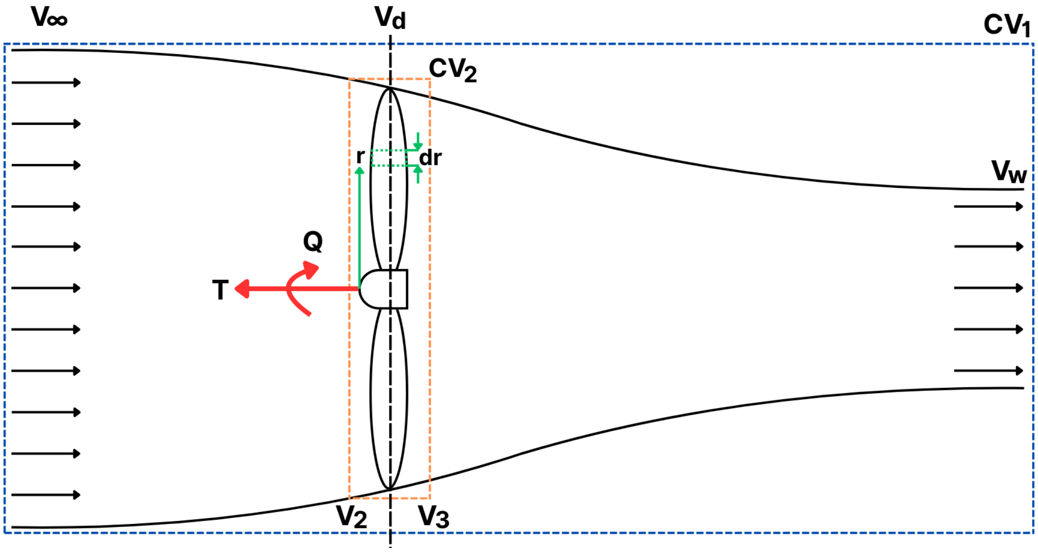

Figure 2.1: Streamtube for Momentum Theory model

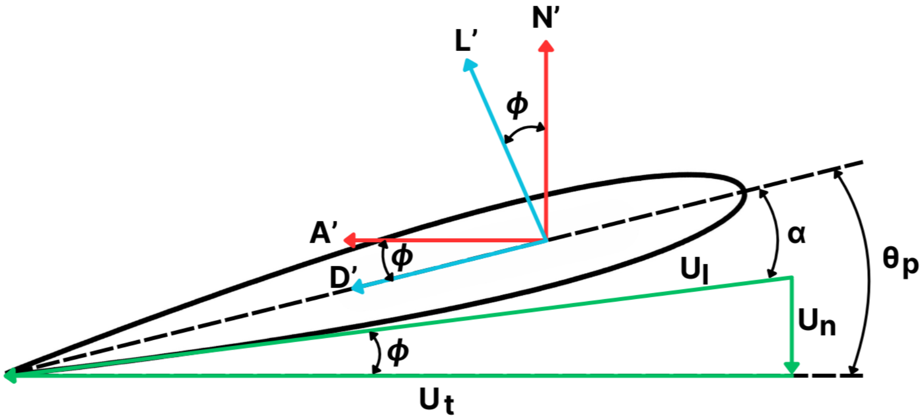

Figure 2.2: Geometric relations of an infinitesimal blade element

2.2.2 Tip Loss Correction

Recall that the derivation of Momentum Theory assumes infinite blades. In order to correct the loading for a propeller of a finite number of blades, Glauert introduced and modified Prandtl's tip loss factor to BEMT. Prandtl initially approximated the circulation of the helical wake as the change in velocity potential over a vortex sheet and defined the correction as the ratio between the circulation of an N-bladed propeller and an infinite-bladed propeller. Glauert subsequently modified the correction to form an interpretation consistent with the application of Blade Element Theory. Glauert defines the correction as the ratio between the induced velocity on an infinite series of plates and the average induced velocity between the plates [25]. This formulation is consistent with Prandt's definition and additionally introduces the local flow angle associated with Blade Element Theory to yield the tip correction most commonly used in BEMT:

$$F = \frac{2}{\pi} \arccos e^{-f} \tag{2.27}$$

with the local correction factor f given by

$$f = \frac{B}{2}(\frac{R-r}{r\phi}) \tag{2.28}$$

R is the total blade radius and r is the local radial length. This correction ultimately models a reduction in lift near the tip of a propeller blade due to an equalization in pressure. The correction factor is subsequently implemented into BEMT through the following modifications of the induction factors:

$$a = \frac{1}{\frac{F4\sin\phi^2}{\sigma C_n} - 1} \tag{2.29}$$

$$a' = \frac{1}{\frac{F4\sin\phi\cos\phi}{\sigma C_t} + 1} \tag{2.30}$$

2.2.3 Modifications for Yaw

Although BEMT is not initially compatible with a propeller at a nonzero yaw angle, modifications can be made to the normal and tangential velocity components to account for the rotation between the flow and propeller plane. The velocity experienced in the propeller plane is comprised of a normal U_n and in-plane U_p component. From the perspective normal to the propeller plane, the blades perceive varying magnitudes of the in-plane component according to azimuthal position in addition to the tangential velocity component from the propeller's rotational speed (Figure 2.3). Therefore, the equations of the normal and tangential velocity components become:

$$U_n = V_\infty \cos\Psi(1 + a) \tag{2.31}$$

$$U_t = (\omega r + V_\infty \sin\Psi \cos\psi)(1 - a') \tag{2.32}$$

Where Ψ is the yaw angle and ψ is the azimuth angle of the propeller blade. In this implementation, the radial component U_r of flow along the blade is ignored.

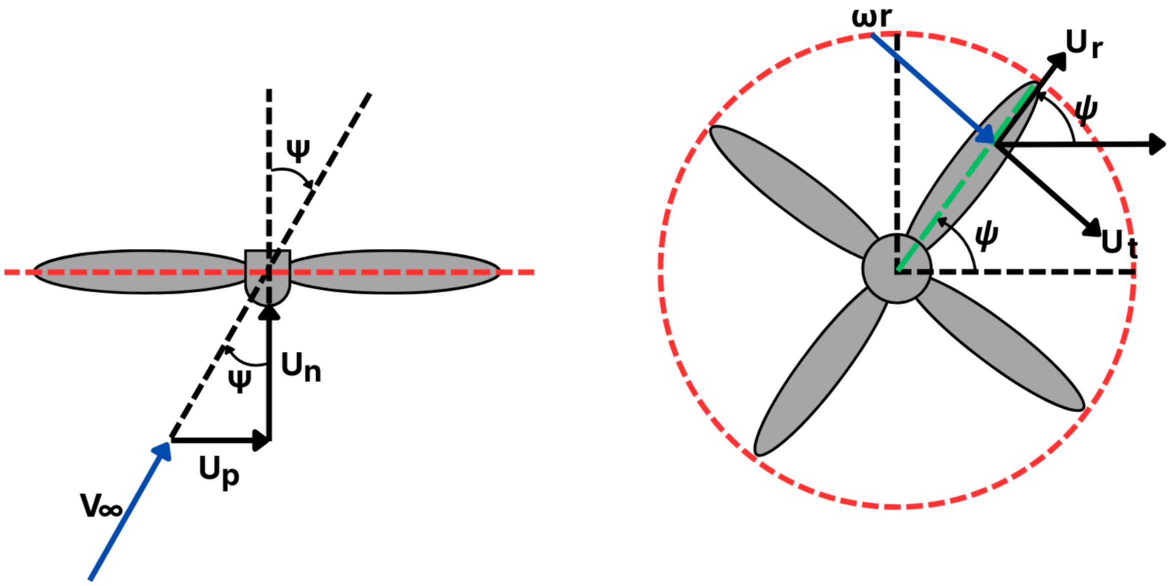

Figure 2.3: Velocity components for a propeller at yaw, viewed in-plane (left) and normal to the propeller plane (right)

2.2.4 Non-Dimensionalized Performance Parameters

Similar to fixed-wing aircraft, UAM vehicle performance is assessed using non-dimensional quantities, allowing for the comparison of generalized performance between different propellers. For rotating-wing aircraft, it is the convention to normalize all velocities by the blade tip speed in hovering flight ($V_{tip} = \omega R$) [15]. Thrust is normalized as the product of the dynamic pressure at the propeller tip and the total propeller disk area, defined as:

$$C_T = \frac{T}{\rho A V_{tip}^2} = \frac{T}{\rho A \omega^2 R^2} \tag{2.33}$$

With the corresponding torque coefficient defined similarly:

$$C_Q = \frac{Q}{\rho A V_{tip}^2 R} = \frac{Q}{\rho A \omega^2 R^3} \tag{2.34}$$

Employing momentum theory for a propeller in hover, the power coefficient is defined as shown in Equation 2.35. However, momentum theory assumes uniform flow and no viscous losses, thus this term is named the ideal power coefficient. It is additionally important to note that because power is related to torque by $P = \omega Q$, numerically $C_P \equiv C_Q$.

$$C_P = \frac{P}{\rho A V_{tip}^3} = \frac{P}{\rho A \omega^3 R^3} = \frac{C_T^{3/2}}{\sqrt{2}} \tag{2.35}$$

Although other loading parameters have a part in defining the efficiency of a propeller in hover, the standard nondimensional measure of static thrust efficiency is the Figure of Merit (FM). FM is defined as the ratio of the ideal power to the actual power required. The actual power required is the measured power which includes viscous effects and other nonideal phenomena that occur in real flight.

$$FM = \frac{P_{ideal}}{P_{actual}} = \frac{C_T^{3/2}}{\sqrt{2} C_P} \tag{2.36}$$

2.3 Propeller Acoustics

Noise sources in rotorcraft are generally categorized into two categories: aerodynamic noise and mechanical noise. The focus of this paper lies in studying the aerodynamic noise of propellers. Aerodynamic noise is defined as the sound generated by the interaction between a solid body and its surrounding fluid medium [12]. Aerodynamic noise can be further separated into two categories based on sound profile: tonal and broadband. Tonal noise is sound that is focused at discrete frequencies typically associated with periodic sources. In contrast, broadband noise is distributed over a wide range of frequencies due to stochastic, unsteady processes.

2.3.1 Tonal Noise

Tonal noise is composed of rotational noise and periodic interactions. Rotational noise includes noise generated from steady blade loading and thickness. Rotating blades impart a pressure distribution upon the surrounding medium, which can be decomposed into two components of force: thrust, acting along the axis of rotation, and torque, acting perpendicular to the axis. This pressure distribution is seen as steady relative to the rotating blades, thus from a fixed point on the disk, the noise source is representative of a fluctuating pressure oscillating at the Blade Passage Frequency (BPF). In addition, noise is generated by the mass displacement of the medium due to the finite thickness of the blades. Noise generated by steady blade loading is generally of higher intensity than thickness noise. However, the intensity of thickness noise is influenced by the rate at which mass is displaced by the blade, therefore its intensity can be comparable to blade loading noise at high tip speeds. Lastly, interactive effects such as Blade Vortex Interaction (BVI) generate periodic noise associated with the interaction between blades and unsteady flow. In the case of BVI, a blade experiences fluctuating forces as it encounters the tip vortices shed by a preceding blade [12]. Similar to the previously mentioned sources, noise associated with BVI occurs at discrete frequencies associated with the BPF.

2.3.2 Broadband Noise

Broadband noise sources primarily consist of propeller self-noise, Turbulence Ingestion Noise (TIN), and Blade-Wake Interaction (BWI) noise. Firstly, propeller self-noise is caused by the interaction of near-wake turbulence and the boundary layer at the trailing edge of a blade. Self-noise can be further characterized by an airfoil's boundary layer profile as described in [4]. Turbulence ingestion noise is attributed to the ingestion of atmospheric turbulent flow and is difficult to model due to the stochastic nature of turbulence [27]. Lastly, BWI noise is attributed to a blade's leading edge interaction with the wake of a preceding blade. While BWI is related to the tip vortices generated by a preceding blade, it also encompasses the fluctuating components around these vortices. As a result, the interaction with each blade passage is random. This leads to BWI manifesting as a dominant broadband noise source, in contrast to BVI, occurring across mid to high frequencies and is of significant presence for a propeller in edgewise flight [11]. The objectives of this research include a greater emphasis on broadband noise sources, given their complexity and relevance to UAM vehicles operating in environments with a high probability of encountering turbulent flows.

2.3.3 Characteristics of UAM Noise

Given their unique designs, UAMs' noise profiles can differ greatly from those of traditional rotorcraft. UAMs typically rely on a greater number of small propellers operating at lower tip speeds. These propellers may function at varying RPM, pitch, and tilt angles from one another, adding an additional dimension of sophistication to their operation. The complex nature of UAM design therefore contributes to multifaceted frequency profiles and introduces intricate aerodynamic interactions that differ from those of conventional aircraft. Potential noise sources associated with UAM are illustrated in Figure 2.4.

The lower tip speeds of distributed propeller utilization lead to a reduction of aerodynamic noise and eliminate motor noise associated with conventional turboshaft engines. However, electric propulsion will inevitably contribute to noise, but with unique characteristics. In conventional rotorcraft, BVI noise is typically dominant in descent. For UAM, BVI noise may be present in vertical or transitional flight when propellers are configured non-axially, however, it is minimized by operating at lower tip speeds. Blade Airframe Interaction (BAI) is more prevalent in UAM due to the close proximity of propellers to the airframe and wings, disturbing the flow across the wings and creating additional noise sources. Conversely, propellers configured behind airframe elements could experience unsteady loading caused by the ingestion of wakes from the body or wings, resulting in Fuselage-Wake Interaction (FWI) noise. While BAI and FWI are expected to be more prevalent in the current proposed UAM designs, the broadband noise generated by BWI and propeller-propeller interaction are considered to be of the most importance [23]. Similar to FWI, propellers positioned downstream will interact with the wakes of propellers upstream resulting in unsteady loading and noise production. The fluctuating nature of these interpropeller and intrapropeller interactions leads to the expectation of prominent broadband noise generation unique to UAM.

In addition to noise sources from intravehicle interactions, the operation of UAM in urban settings introduces additional complex interactions of the vehicle with its environment. The expected proximity to buildings may shed turbulence that is not yet well understood, resulting in TIN. The fluctuating flow field of UAM operating environments inevitably introduces unsteadiness that is propagated through each propeller interaction, enhancing the intensity of BWI and propeller-propeller interaction. However, the ability to individually configure propellers can be leveraged to optimize trim states for noise mitigation. Additionally, buildings made of acoustically reflective materials and atmospheric conditions can influence the propagation of noise generated by UAM [23]. This introduces flight path optimization as another area of concern. Ultimately, the first step in mitigating noise emissions from UAM vehicles is to understand the fundamental sources and interactions associated with the proposed propeller geometry.

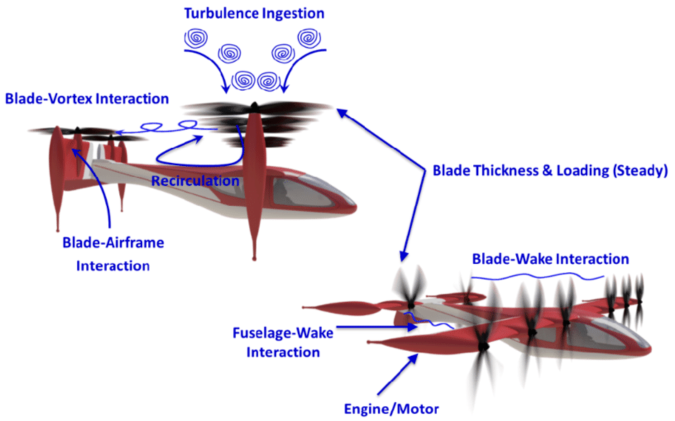

Figure 2.4: Potential noise sources of a UAM vehicle (adapted from Rizzi et al.)

Chapter 3

Apparatus and Instrumentation

3.1 Virginia Tech Stability Wind Tunnel

All data presented in this work were acquired from experimentation utilizing the Virginia Tech Stability Wind Tunnel (VTSWT) in its anechoic configuration. High flow quality, low background noise, and acoustic measurement capabilities make this facility an ideal testing facility for the study of propeller performance and acoustic experimentation.

The Virginia Tech Stability Wind Tunnel is a continuous, single-return, subsonic wind tunnel with a test section cross-section of 1.85 m x 1.85 m and a length of 7.3 m located inside a hermetically sealed facility, shown in Figure 3.1. A 3-degree diffuser is located at the downstream end of the test section with eight 0.16 m high vortex generators arranged at intervals of 0.78 m around the floor, ceiling, and entrance side walls to mix momentum into the boundary layer, minimizing flow separation and instability. Flow is generated by a 4.3 m diameter fan of 8 blades, powered by a 0.45 MW variable speed DC motor which is capable of producing flow speeds up to 80 m/s, corresponding to a Reynolds number of 5,000,000 per meter [22]. The fan is controlled by a custom-designed Emerson VIP ES-6600 SCR Drive which regulates the rotational speed up to a maximum of 600 RPM. The precisely regulated DC power source eliminates cyclic fluctuations in flow velocities and vibrations that can induce turbulence. Downstream of the fan is an air exchange tower that is open to the atmosphere, which aids in stabilizing flow temperature. Following the exchange tower, the circuit turns 180 degrees, directing the flow into a settling chamber of dimensions 5.5 m x 5.5 m. This chamber includes seven turbulence-reducing screens followed by a 9:1 contraction nozzle, further reducing turbulence and accelerating the flow into the test section. The combination of turbulence screens and contraction configuration results in minimal free-stream turbulence on the order of 0.03% inside the test section. The wind tunnel test section has two interchangeable layouts: aerodynamic and anechoic.

3.1.1 Anechoic Configuration

This experiment utilizes the SWT's anechoic configuration in which the traditional hard-wall test section is replaced with acoustically treated floor and ceiling panels. These panels are constructed of perforated aluminum plates covered by Kevlar sheets, which are stretched across the flow surface. Additionally, foam wedges are placed within the floor and ceiling to further enhance acoustic treatment. The sidewalls feature large openings covered with tensioned plain-woven Kevlar fabric, functioning as acoustic windows. These windows allow sound waves to pass through while effectively containing the flow. Due to this characteristic of Kevlar, the test section acts acoustically as if it were an open-jet test section, without producing a significant shear layer. Behind each window is a 6 m x 2.8 m x 4.2 m anechoic chamber used for housing acoustic instrumentation, protected from the flow. These chambers are designed to minimize reflection and maximize signal-to-noise ratio (SNR). This configuration results in the test section being anechoic down to 180 Hz [5]. A schematic of the full anechoic configuration is shown in Figure 3.2

Located above the ceiling of the test section is a Kinematics model ZE14C slew drive turntable system, capable of applying torques up to 1000 N-m with a resolution of ±0.01°. A Renishaw ENERCON10 linear magnetic encoder system measures the turntable's position. Fitted to the turntable is a lathe chuck that allows for the attachment of test section models, typically used to vary the angle of attack of airfoils. In this experiment, the turntable system is utilized to adjust the yaw angle of the experimental propeller assembly.

3.1.2 Tunnel Reference Measurements

For each measurement condition, reference conditions of the testing environment were measured using the facility's integrated pressure and temperature systems. Pressure measurements from ports within the settling chamber and contraction section of the Stability Wind Tunnel were recorded using an Esterline 9816/98RK pressure scanner, with a rated accuracy of 0.05% and a range of ±2.5 psi. These measurements were calibrated to ensure that the freestream velocity in the test section is accurate within ±0.1 m/s. Ambient temperature was monitored using an Omega 44004 Thermistor, installed in the wind tunnel contraction, with a rated accuracy of ±0.2 °C.

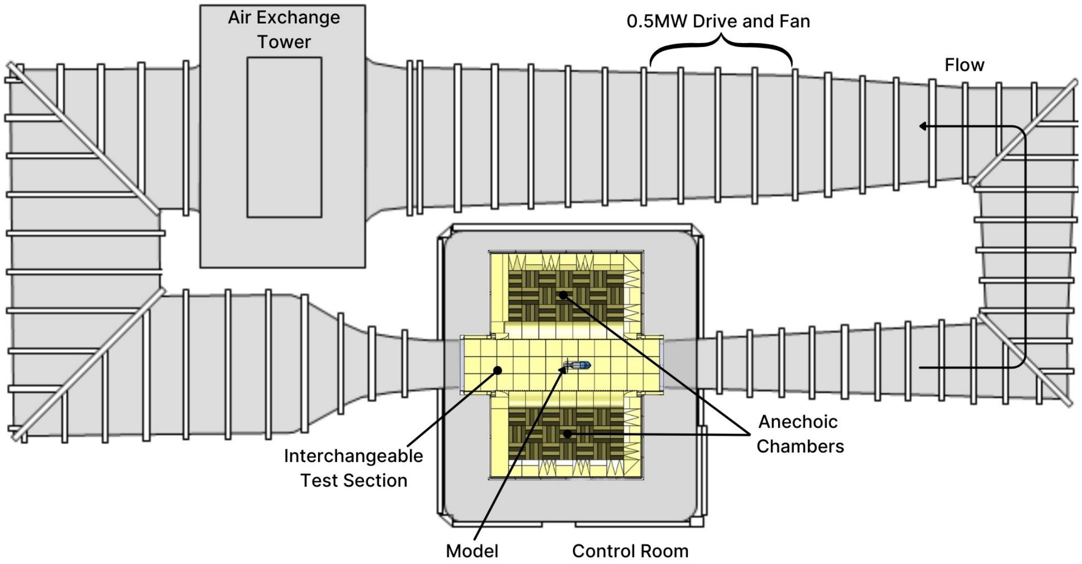

Figure 3.1: Top view schematic of the Virginia Tech Stability Wind Tunnel

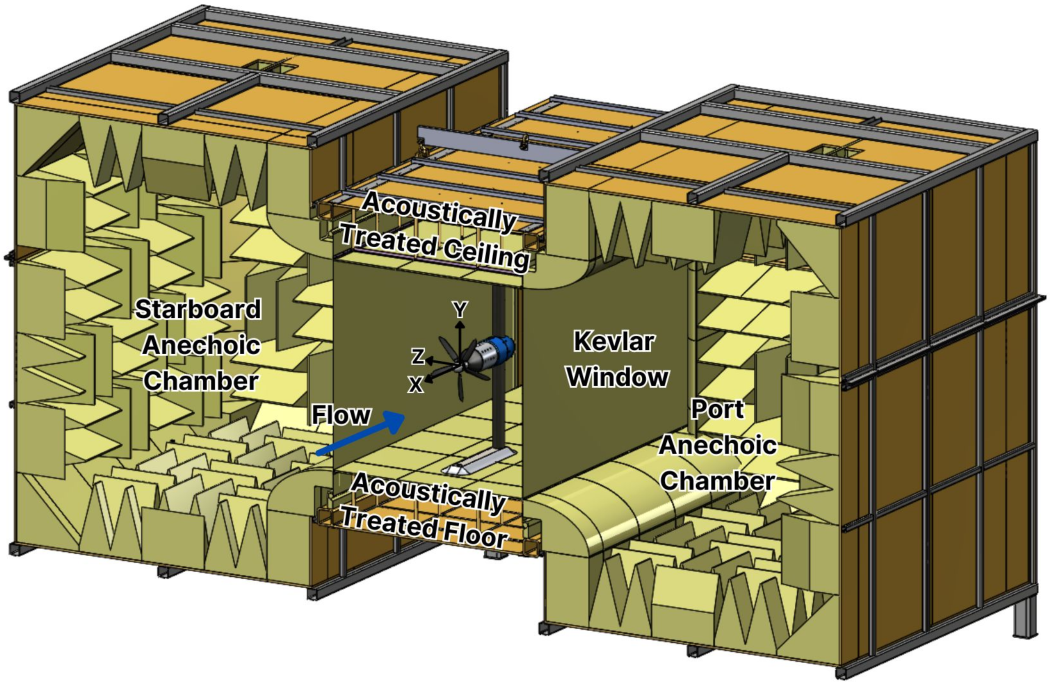

Figure 3.2: Sectional view of the Virginia Tech Stability Wind Tunnel test section in full anechoic configuration

3.2 Microphone Phased Array

Acoustic measurements in the SWT are acquired by a 251-channel microphone array mountable in either anechoic chamber. Designed by AVEC Inc, the array is constructed of 251 custom GRAS 0.5 inch free-field microphones type 40PH-S5. The microphones have a dynamic range of 32 to 135 dB(A) and a sensitivity of 50 mV/Pa. Data is acquired by a custom high-speed data acquisition system, also designed by AVEC, at a sampling rate of 51200 Hz for 32 seconds [2]. AVEC software and MATLAB were used in this experiment to process collected microphone array data.

The microphone array's modular design accommodates various testing configurations inside the Stability Wind Tunnel. The array is comprised of four identical interlocking sub-arrays, each in a spiral pattern (Figure 3.3). This unique spiral pattern is designed to eliminate redundancy in microphone spacing by slightly rotating each spiral relative to the others. The microphone spacing ranges from a minimum of 29.8 mm to a maximum of 3.82 m. The array extends 3.66 m in the streamwise direction and 1.75 m in the vertical direction. Capabilities of the microphone array include high-resolution acoustic maps with full aperture and generation of beamforming maps, using each spiral section as an individual sub-array while achieving consistent source resolution in the streamwise distribution with max aperture. Each sub-array can be separated and placed in either anechoic chamber or as a single planar array, while simultaneously sampling at a frequency of 51200 Hz regardless of the configuration [2]. In this experiment, the microphone array was configured as a single planar array inside the starboard anechoic chamber, as illustrated in Figure 3.4.

Figure 3.3: 251-channel microphone array configured in a single plane in the port side anechoic chamber of the Virginia Tech Stability Wind Tunnel

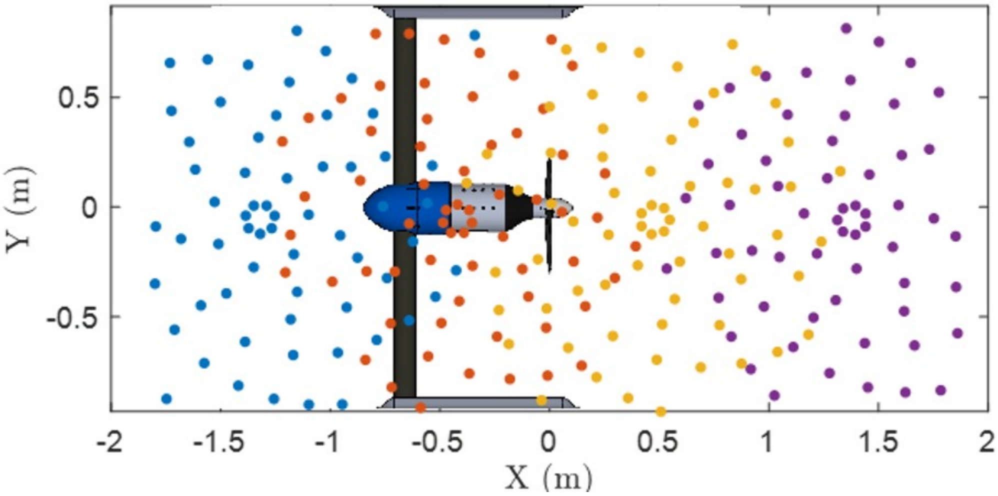

Figure 3.4: 251-channel microphone array plotted relative to the propeller model in axial flight, with each individual spiral highlighted, from the perspective of the starboard side anechoic chamber

3.3 Force Measurement Instrumentation

Force measurements were obtained using a JR3-75E20A4 force-torque sensor. This JR3 sensor is a monolithic aluminum load cell, containing foil strain gauges to sense applied loads. Signals from the strain gauges are amplified and consolidated to create analog representations of resultant loads in six components. The six components include the force load along each of the three axes and their corresponding moment about each axis. The sensor's axes are oriented such that the X and Y axes lie in the plane of the sensor body, with the Z axis perpendicular to both, forming a right-handed coordinate system, as shown in Figure 3.5 below. The geometric center of the sensor serves as the reference point for all load measurements. The sensor was mounted on the rear end of the experimental propeller, with the propeller plane parallel to the X-Y plane of the sensor. In this configuration, F_z and M_z correspond to the measurements of thrust and torque generated by the propeller. The sensor measurement ratings can be seen in Table 3.1 and Table 3.2.

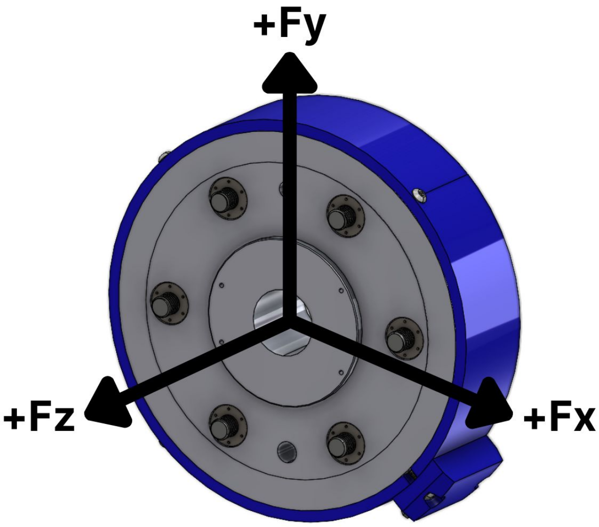

Figure 3.5: JR3 force-torque sensor coordinate system as seen from the mounting side

Table 3.1: JR3 sensor force component ratings

Component	**Range (N)**	**Digital Resolution (N)**	**Nominal Accuracy (N)**
F_x	±500	0.065	±1.25
F_y	±500	0.065	±1.25
F_z	±1000	0.125	±2.50

Table 3.2: JR3 sensor moment component ratings

Component	**Range (Nm)**	**Digital Resolution (Nm)**	**Nominal Accuracy (Nm)**
M_x	±100	0.125	±0.25
M_y	±100	0.125	±0.25
M_z	±100	0.125	±0.50

Chapter 4

Experimental Propeller Design

The propeller assembly used in this experiment was designed to be analyzed in a series of wind tunnel experiments. The propeller is approximately 21% scale of a single propeller from Joby's first full-scale prototype from 2017. The Joby vehicle features six 5-bladed propellers of 2.9 meters in diameter. The propeller was scaled with a tip Mach number matching that of the full parameters at the hover condition, provided by Joby Aviation, and a required tip-to-tip diameter of 24 inches. Coefficients of thrust and torque were calculated with the full-scale parameters and a figure of merit of 0.725 (Table 4.1), using Equation 2.33, Equation 2.34, and Equation 2.36. These coefficients were then used to determine the predicted performance of the scaled propeller, using its respective scaled RPM and diameter. Full-scale and scaled performance values are listed in Table 4.2. Among designing to meet these performance requirements, 3 main design criteria were required:

1. Enable variable blade pitch angle
2. Support variable yaw to achieve axial and edgewise flight
3. Measure thrust and torque

The following sections describe key design elements and provide a comprehensive overview of the design (see Figure 4.1). All parts, excluding the propeller blades, were fabricated at Virginia Tech.

Table 4.1: Calculated performance coefficients using the full-scale performance parameters of the Joby prototype vehicle

Coefficient	**Value**
C_t	0.0335
C_q	0.00598
Figure of Merit	0.725

Table 4.2: Full-scale and scaled propeller performance parameters for hover condition

Parameter	**Full-Scale**	**Scaled**
Diameter (m)	2.9	0.6096 ($24in$)
RPM	800	3806
Thrust (N)	4000	178
Torque (Nm)	1035	9.62

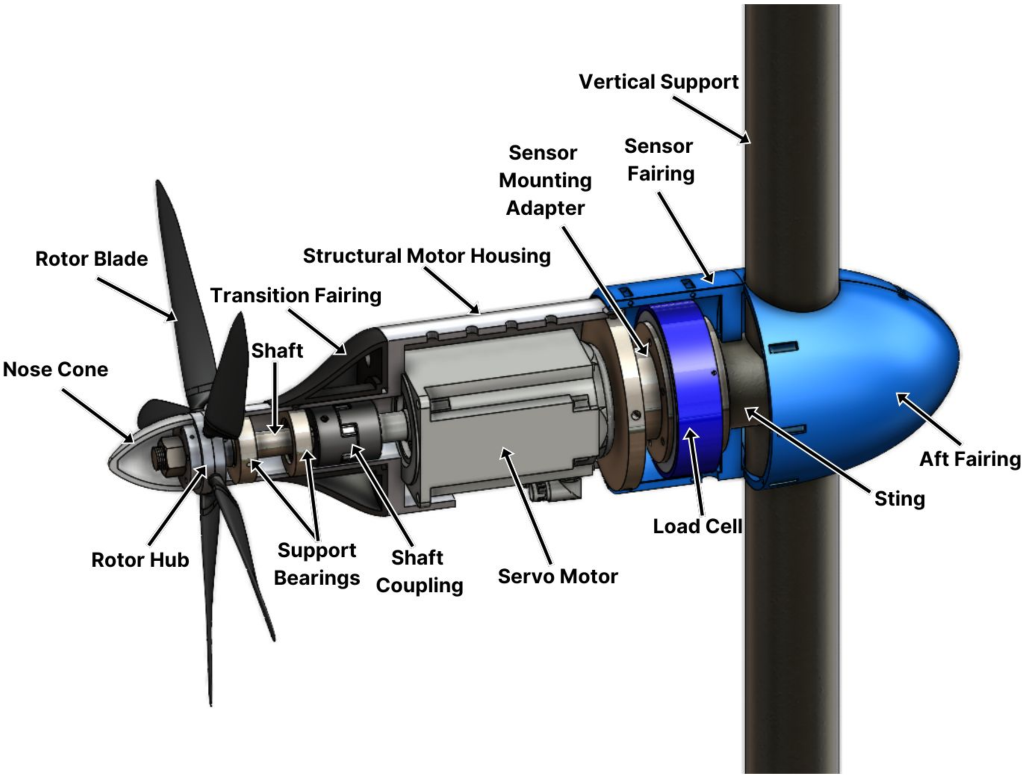

Figure 4.1: Sectional View of the designed propeller assembly

4.1 Blade and Hub

The blade geometry for the scaled experimental propeller was provided by Joby Aviation, and modeled after the blades featured in the Joby 2017 prototype propeller. The blades were fabricated individually, separate from the hub. Fabrication involved injection molding using Complēt® LCF40-PA66, a composite material consisting of Nylon 66 resin reinforced with long carbon fiber. This method and material were chosen to provide substantial strength while maintaining a lightweight profile. A total of seven blades were fabricated; however, some minor imperfections on the blade surfaces were observed, therefore five optimal blades were selected upon evaluation for use in experimentation. The blade span from root to tip is 11.05” with a maximum chord length of 1.979” at 40% radius as well as thickness-to-chord ratios of 17% and 10% at the root and tip, respectively. The blade pitch angle for the hover condition, as specified by Joby, is approximately 16 degrees at 75% blade radius. Additional blade pitch configurations are in reference to the airfoil section at 75% blade radius (Figure 4.2). The chord and twist distributions of the blade geometry, measured at 20 radial positions along the span, are illustrated in Figure 4.3.

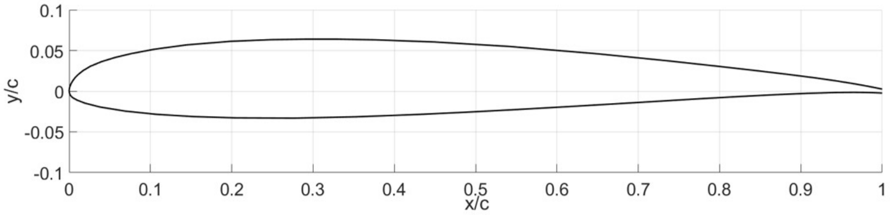

Figure 4.2: Airfoil section at r/R = 0.75, the reference point for defining blade pitch angle

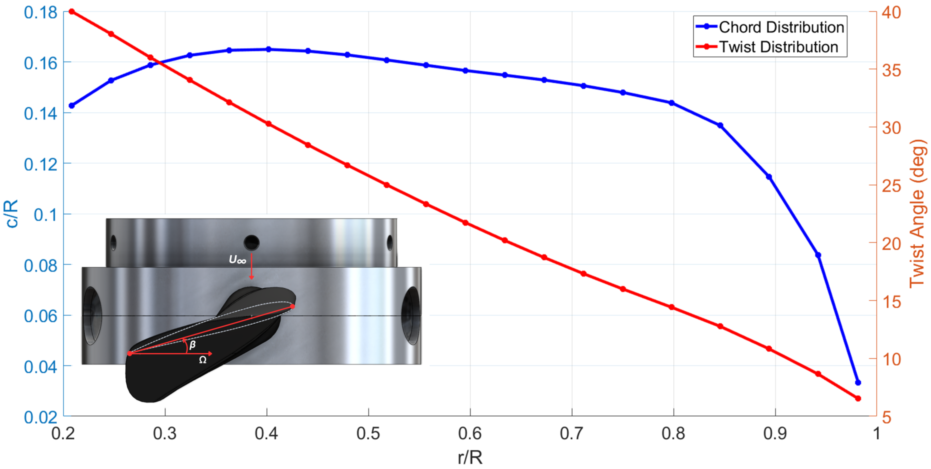

Figure 4.3: Chord and twist distribution of the experimental propeller blade geometry measured at 20 radial positions along the span

The assembled propeller as designed and fabricated is shown in Figure 4.4. It is constructed with two 3.5-inch diameter hub plates, one front and one back, each featuring cutouts that match the blade root geometry. These cutouts allow the blades to fit seamlessly between the plates, securely held by clamping the plates together and fastened by a circular pattern of five bolts. The hub plates include a 1-inch diameter bore and keyway for coupling to the shaft. The forward plate has an additional 3-inch diameter extrusion for mounting the nose cone. The nose cone is composed of Delrin and affixed to the front hub plate extrusion by 4 radially positioned counterbore bolts. The cylindrical root of the blades allows for each to be individually rotated to achieve varying blade pitch angles. On the back hub plate, through holes were made to enable the use of set screws at the blade root to secure each blade at the desired pitch angle upon adjustment. An exploded view highlighting the assembly elements is shown in Figure 4.5.

Accurate variable blade pitch was achieved by designing and fabricating a pitch calibration plate, seen in Figure 4.6. This calibration plate consists of a 2.5" tall support, doubling as a stand and mock shaft. This enables the propeller to remain secure in a precise location relative to pins at a specifically selected point along each blade. These pins are positioned coincident with the chordline of the airfoil section at the 75% radial position, towards the trailing edge. A set of five pins, one for each blade, were fabricated at heights corresponding to the distance from the plate to the lower surface of the blade for a given blade pitch angle. Pin heights were determined using the 3D CAD model for pitch angles of 4, 8, 12, 16, 20, and 24 degrees. To adjust the blade pitch angle, the propeller is first positioned on the stand with the pins corresponding to the desired pitch fastened to the plate. Then, with the set screws loosened, the blades can be manually adjusted by hand until the lower surface makes contact with the pins. The set screws are then tightened to secure the blade at the desired pitch angle.

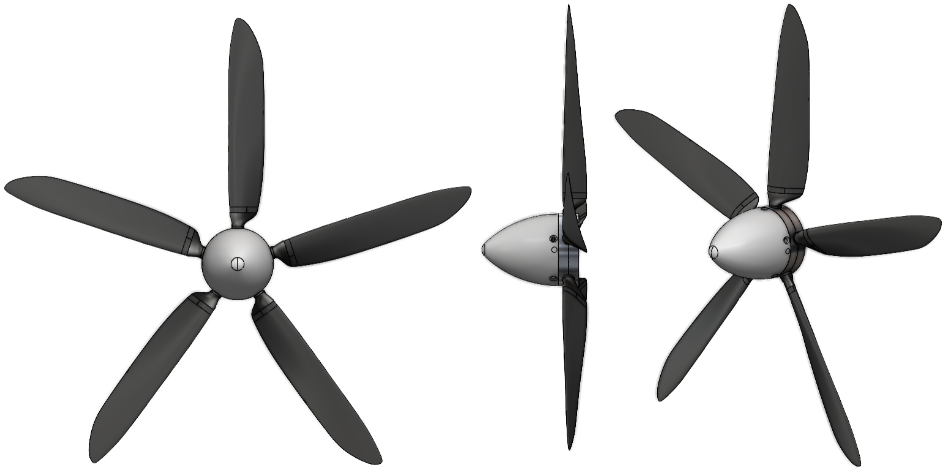

Figure 4.4: 21% scale propeller designed for experimentation in the VTSWT

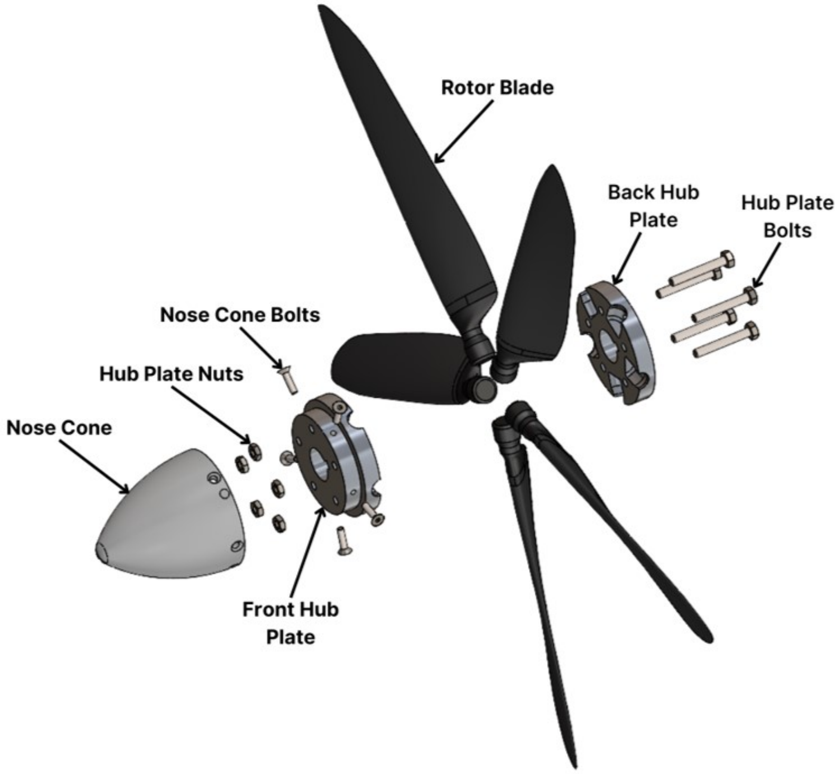

Figure 4.5: Exploded view of the 21% scale propeller

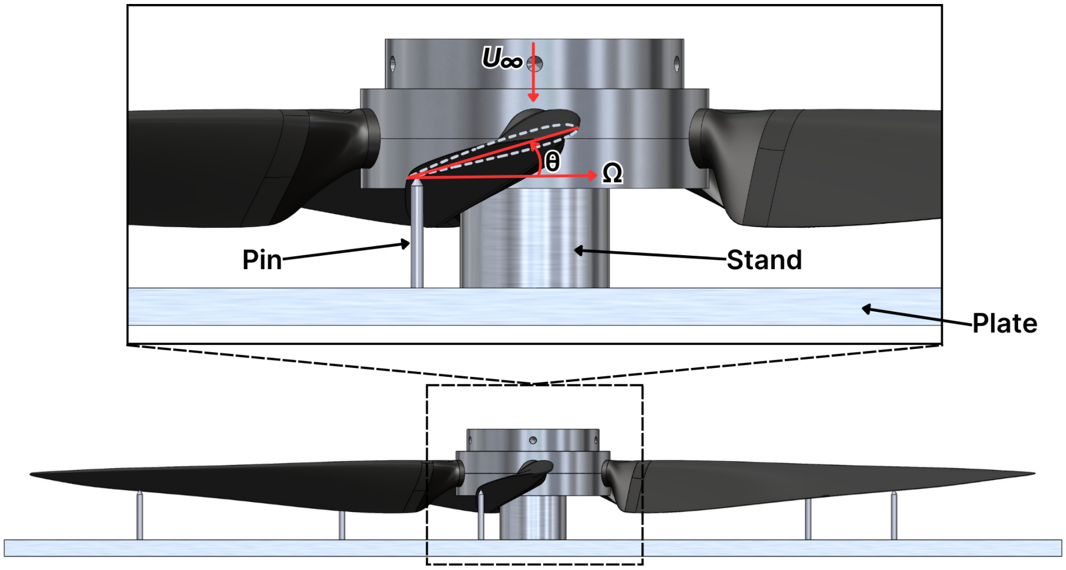

Figure 4.6: Propeller blade pitch calibration plate

4.2 Shaft and Drive

The propeller is attached to a steel shaft coupled to and driven by an AKM-64P-ACCNDA00 Kollmorgen servo motor controlled by an S61200 servo drive. The motor is rated for continuous torque output between 8 and 21 Nm at speeds up to 6000 RPM. It contains a built-in encoder that determines the angular position of the drive shaft and measures the RPM. In this experiment, the motor speed was controlled using the provided servo drive software and ran for speeds ranging between 1000 to 4000 RPM.

The propeller shaft is mated to the servo motor with a Lovejoy spider coupling and supported by two sealed ball bearings to reduce noise. The shaft is 1 inch in diameter with a 1/8th-inch step increase in diameter extending 2 inches in length starting, 2 inches from where the shaft couples to the motor. This step allows for the bearings to be pressed coincident with the stepped surface from the front and rear of the shaft. Each bearing is secured in place by custom-built steel collars that fasten to a structural housing with 4 radially mounted bolts. Utilizing sealed, pressed bearings results in minimal mechanical noise. A shaft collar and bolt are used on the end of the shaft to secure the assembled propeller in the axial direction. The shaft design is illustrated in Figure 4.7. The shaft mechanism and drive system are installed in a custom-built aluminum housing fitted with a 3D-printed fairing to reduce drag on the motor housing which can be seen in Figure 4.1. The motor is mounted to the face of the structural housing such that the forces on the assembly are isolated to ensure accurate measurements by the load cell.

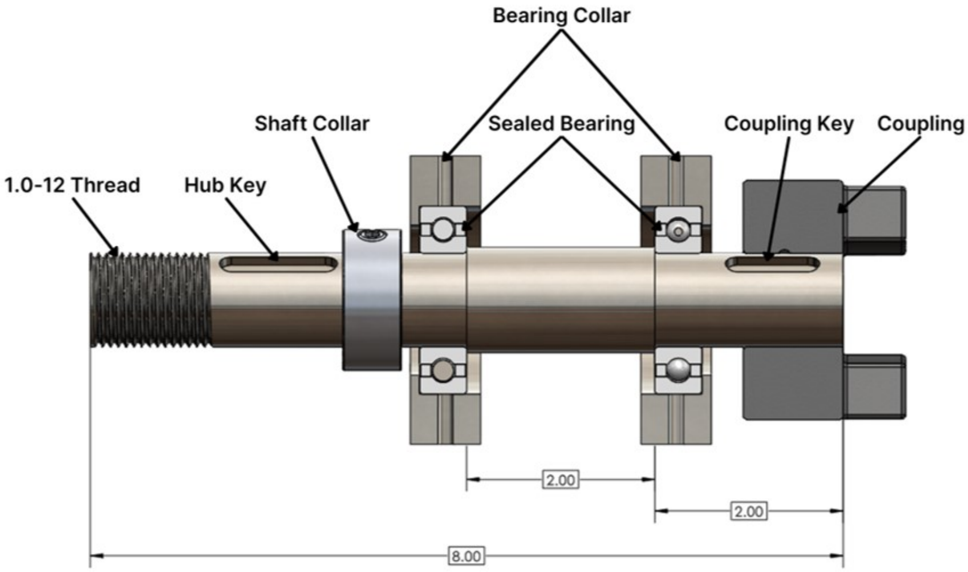

Figure 4.7: Partial cutaway of the shaft mechanism. Dimensions are in inches

4.2.1 Flow Disturbance Study

When studying the propeller in an edgewise flight configuration, the propeller shaft is positioned perpendicular to the test section walls, constraining the length of the propeller assembly to the half-width of the test section, thus requiring the length of the shaft to be minimized. Upon its design, a potential flow study was conducted to determine the optimal distance from the motor housing to the propeller plane while accommodating the dimensions of the individual components of the shaft mechanism and reducing the disturbance due to the structural housing downstream of the propeller. Coordinates for the profile of the housing assembly were generated and revolved 360 degrees to create a 3D model for calculating surface pressure distributions and velocity vectors using a doublet panel method. This calculation did not include the propeller blades or any additional downstream structures than what is illustrated in Figure 4.8 below.

A velocity contour, seen in Figure 4.9, was computed at the propeller plane to determine the degree to which the freestream flow is disturbed in ideal flow. It was determined that an acceptable level of disturbance near the propeller tip was $\leq 1\%$ deviation from the freestream velocity in axial flight. As a result of this study, the optimal shaft length was determined to be 8 inches, which results in a change in freestream velocity of 0.3% at the propeller tip.

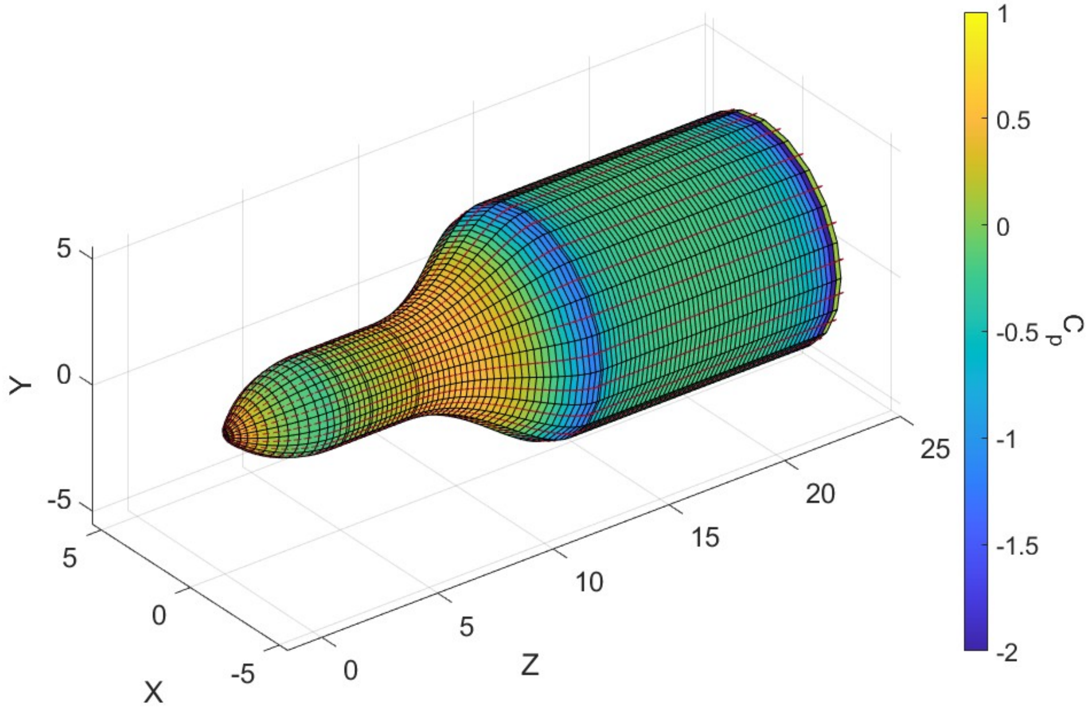

Figure 4.8: Coefficient of pressure of the 3D generated housing assembly model

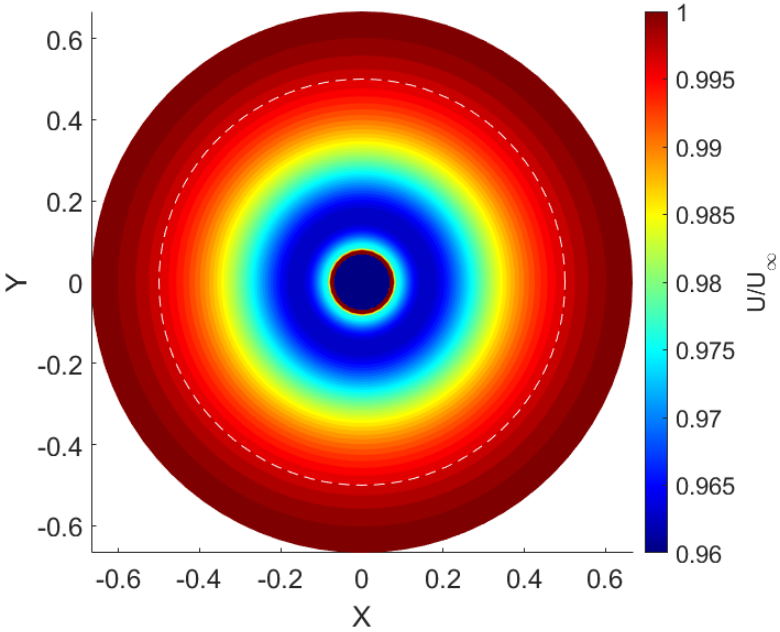

Figure 4.9: Velocity magnitude contour located at the propeller plane. The propeller tip is illustrated by the white dashed line

4.3 Variable Yaw Mount

The structural mount and yaw system for the propeller assembly (Figure 4.10) were designed to facilitate installation within the stability wind tunnel test section and to adjust the yaw angle of the entire assembly as required. A c-shaped geometry was used to isolate the propeller from structural members. Two horizontal steel beams of dimension 2x4x30 inches are connected by a 4-inch diameter vertical pipe. This structure spans 71.5 inches in height, nearly the full height of the test section, with a 1 cm gap between the horizontal beams and the floor/ceiling. This gap is filled by a foam sheet with Teflon sheets on the upper and lower surface to allow for the beams to slide flush with the floor and ceiling. Additionally, fairings were designed and fixed to each beam to reduce flow disturbances and noise. Each horizontal beam features shafts extending vertically outside of the test section which were fixed to lathe chuck clamps. The shafts are machined with three flats that allow for a non-slip connection to each jaw of the chuck, minimizing unwanted rotation. The chuck housed in the ceiling is attached to the SWT turntable, while the chuck in the floor is attached to a bearing, resulting in synchronous rotation on each end of the mount. This enables the structural mount to be rotated, ultimately varying the yaw angle of the propeller assembly. Extending from the middle of the vertical pipe is a horizontal sting. The length of the sting is 1.275 inches which aligns the propeller plane with the yaw axis, ensuring the propeller remains at the center of the test section upon rotation. Mounted to the sting is the JR3 load cell used for measuring the thrust and torque of the propeller assembly. The full propeller assembly is then mounted to the sensing surface of the load cell by another custom-built adapter. The load cell is enclosed in a custom-designed 3D printed fairing, carefully shaped to prevent any forces from being transferred from the propeller, while ensuring smooth airflow across the surface. In this experiment, the yaw angle is defined as the angle between the propeller axis and the freestream velocity. Zero-degree yaw (axial flight) is defined by the propeller thrust vector parallel to the flow and 90-degree yaw (edgewise flight) is defined by the propeller thrust vector perpendicular to the flow, illustrated in Figure 4.11. In this experiment, the yaw angle is representative of the vertical tilt angle associated with UAM and VTOL aircraft.

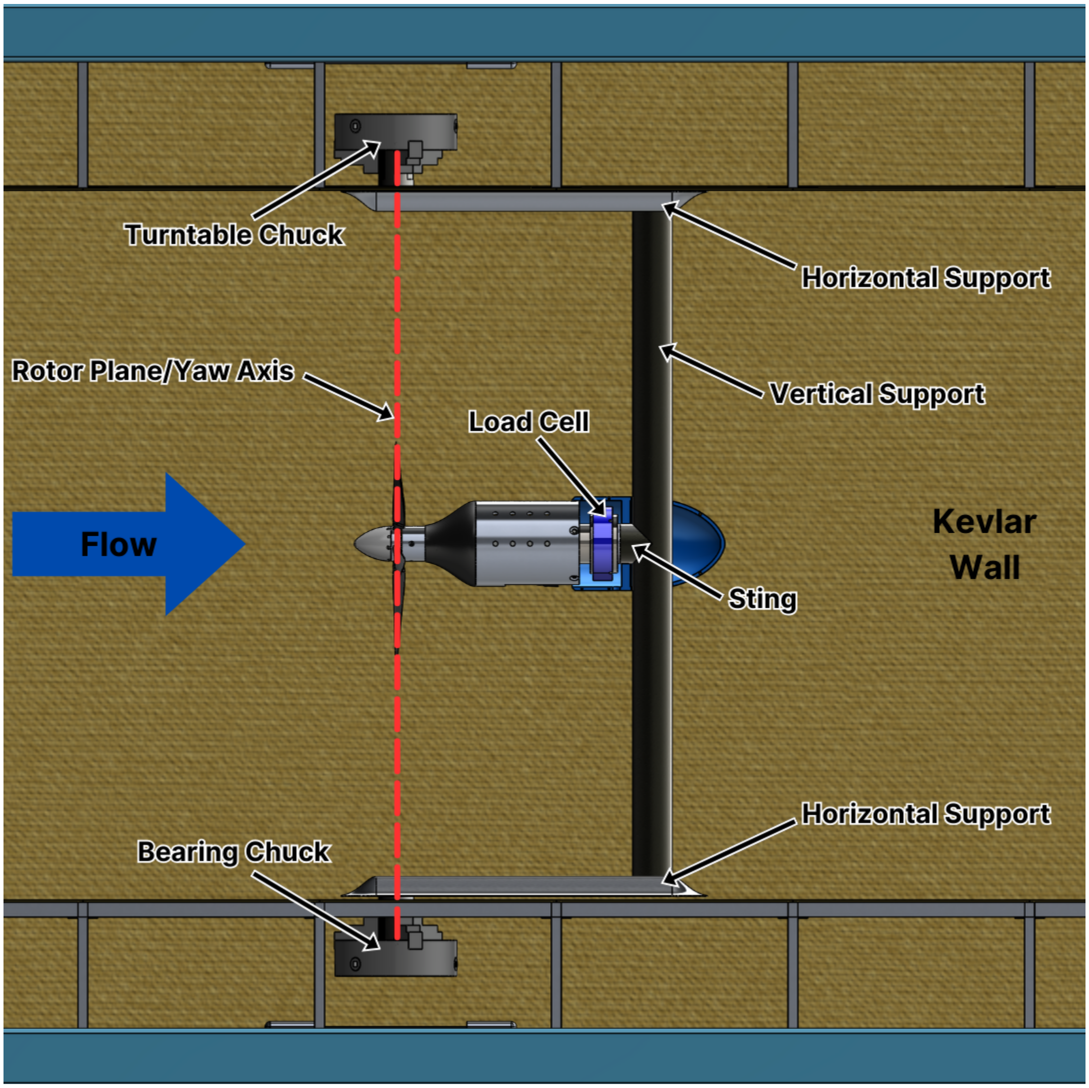

Figure 4.10: Section View of the propeller assembly in the SWT test section highlighting components of the structural mount

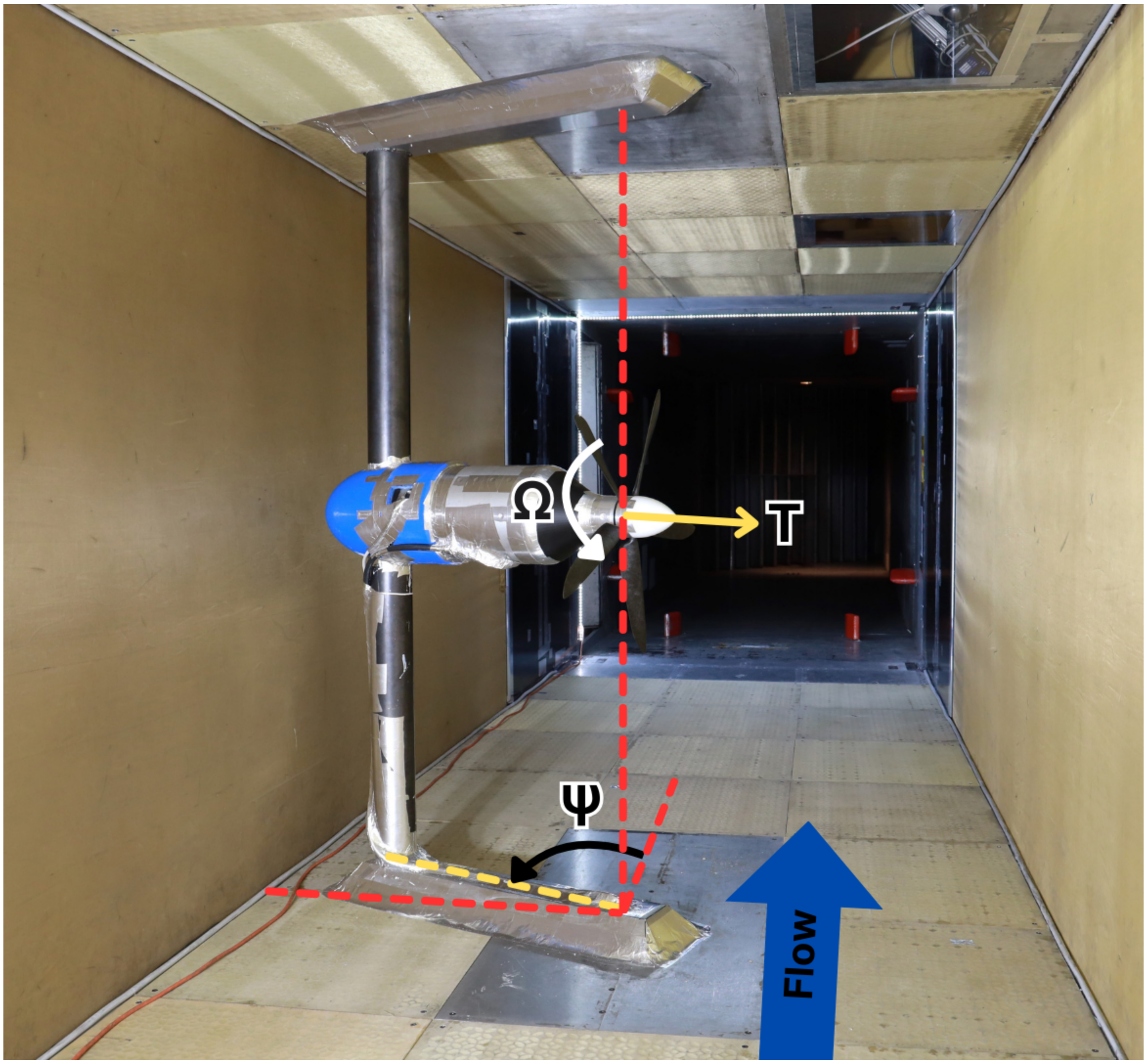

Figure 4.11: Experimental propeller assembly installed in SWT test section highlighting the yaw reference angle

Chapter 5

Results and Analysis

Experimentation was performed with the propeller installed in the VTSWT at yaw angles of 0, 70, 80, and 90 degrees for blade pitch angles of 16 and 20 degrees. 0° refers to the axial flight condition and 90° for edgewise flight. 70° and 80° were examined to analyze the transition state between axial and edgewise flight. Each configuration was investigated for inflow velocities ranging from 0 to 25 m/s. At each condition, force and acoustic data were collected across a range of rotational speeds, from the zero-torque condition up to 4000 RPM, in increments of 200 RPM. Additional data points were taken at the approximate RPM resulting in $\frac{1}{8}$, $\frac{1}{4}$, and $\frac{1}{2}$ of the predicted hover thrust. Each testing condition can be seen in Table 5.1. The following sections provide a comprehensive analysis of the collected performance and acoustic data.

Table 5.1: Test Matrix for the SWT experimentation. Inner cell values state the inflow velocities for the given configuration in m/s.

	Yaw (deg)			
Blade Pitch (deg)	**0**	**70**	**80**	**90**
16	0,10,20,25	0,10,20	0,10,20	0,10,20
20	0,10,20,25	0,10,20	0,10,20	0,10,20

5.1 Performance Analysis

The analysis in the following section details the aerodynamic performance of the experimental propeller. Performance was evaluated using the force data measured from the load cell mounted to the rear of the propeller. Data is comprised of the loads measured about the propeller's rotational axis, with thrust corresponding to the force acting normally on the rotational plane, and torque to the moment about the rotational axis. Measurements were corrected due to what is presumed to be current drifting in the load cell associated with high operating temperatures. This was achieved by subtracting a linear interpolation of tare values from the acquired data points. Additionally, the uncertainties in thrust and torque measurements are derived from the nominal accuracy specifications of the JR3 load cell, defined as 0.25% of the measurement range and previously presented in Table 3.1 and Table 3.2, respectively. Thrust and torque measurements are presented across a range of rotational speeds for each testing condition and are additionally conveyed as calculated normalized performance parameters. Results are presented for the axial flight condition and subsequently compared to cases of non-axial flight.

5.1.1 Axial Flight

In the axial flight condition, the propeller axis is oriented parallel to the flow (Figure 5.1). From Figure 5.2, it is observed that thrust and torque increase proportionally to the square of the rotation speed. This relation is exhibited in Equation 2.20 - Equation 2.22 through the relationship of the local velocity, U_l, to the tangential velocity, U_t, in Equation 2.18. Furthermore, it is evident that as the inflow velocity increases, the thrust and torque produced by the propeller both decrease. This is expected because as the inflow velocity increases, the relative airspeed experienced by the propeller decreases, resulting in a lower angle of attack, α, and consequently a reduction in thrust. In contrast to the variation with inflow velocity, as the blade pitch angle of the propeller increases, we see an increase in thrust and torque, as presented in Figure 5.3. This occurs because a higher pitch angle leads to a larger angle of attack, which increases lift and ultimately results in a greater production of both thrust and torque.

Figure 5.1: Scaled propeller in the axial flight configuration ($\Psi = 0°$)

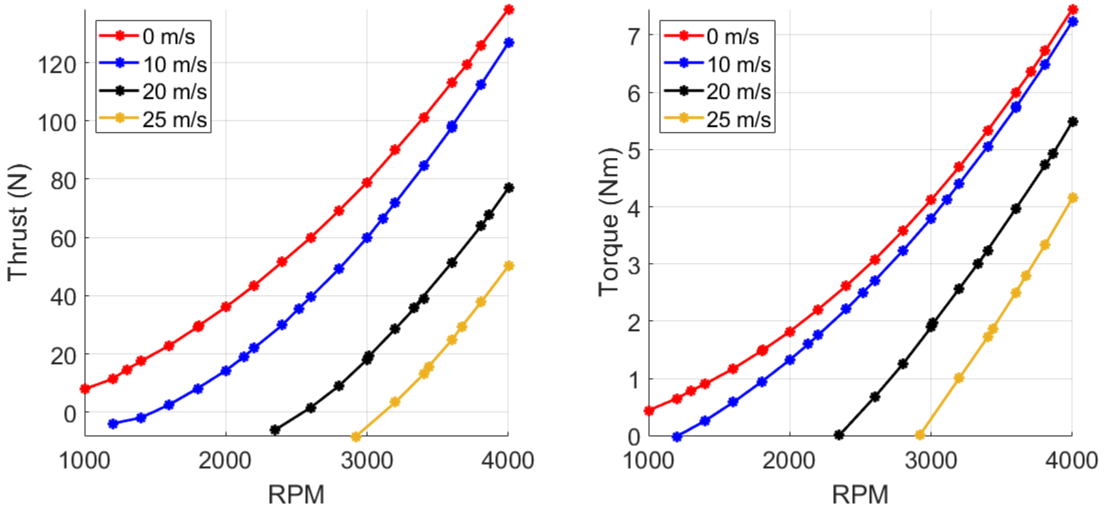

Figure 5.2: Thrust and torque vs RPM measured at varying inflow velocities for the axial flight configuration with a blade pitch angle of 16°

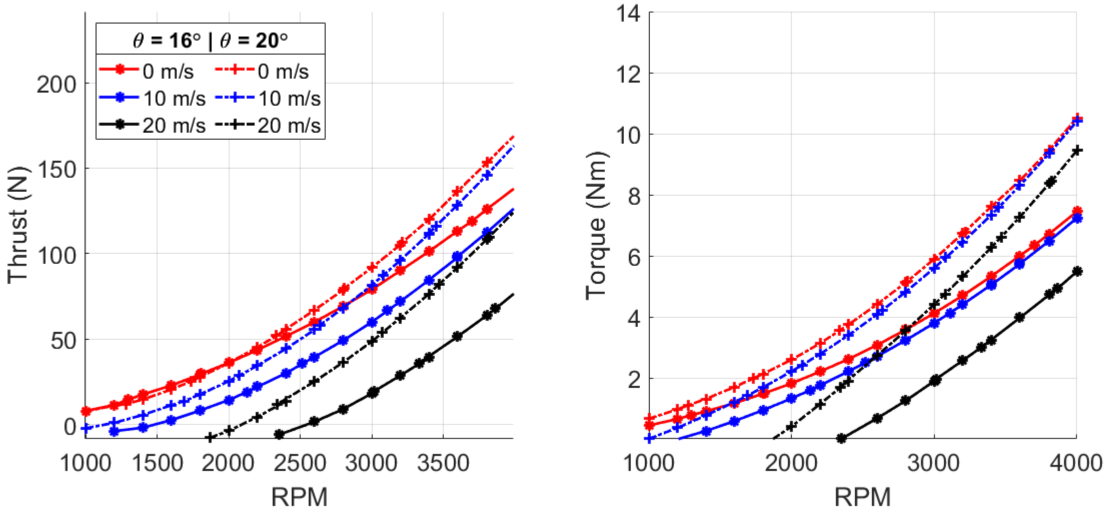

Figure 5.3: Thrust and torque vs RPM measured at varying inflow velocities and blade pitch angles for the axial flight configuration ($\Psi = 0°$)

5.1.2 Non-Axial Flight

In non-axial flight conditions, the propeller axis is oriented at yaw angles of 70°, 80°, and 90° relative to the flow. The edgewise flight condition ($\Psi = 90°$) can be seen in Figure 5.4. In Figure 5.5, it is evident that the thrust and torque increase as the yaw angle increases. It can be shown using Equation 2.31 from Blade Element Momentum Theory that for a propeller in non-axial flight, the normal component of velocity, U_n, is reduced as compared to axial flight. The freestream velocity contributes to the tangential component of velocity, U_t, where it increases in the advancing region ($0° < \psi < 180°$) and reduces in the retreating region ($180° < \psi < 360°$), as shown in Equation 2.32. For a constant freestream velocity, as the yaw angle increases, the subsequent modifications to the flow components result in a reduction of the inflow angle, ϕ, which in turn increases the local angle of attack, and consequently the thrust and torque. Additionally, Figure 5.6 indicates that for a given yaw angle, the thrust and torque increase with freestream velocity. This result is in contrast to the trend presented for the axial flight condition. This provides valuable insight into the performance of a single propeller in nonaxial flight.

Normalized performance coefficients were computed with the acquired data to gain a further understanding of the distinctions between axial and non-axial flight. Coefficients of thrust (C_T) and torque (C_Q) were computed using Equation 2.33 and Equation 2.34, then plotted with the ratio of inflow velocity to tip velocity (U_∞/U_{tip}). In Figure 5.7, U_∞/U_{tip} between 0.16-0.28 corresponds to a range of operating RPMs at constant 20 m/s inflow velocity. In axial flight, the normalized performance parameters both decrease towards zero as U_∞/U_{tip} increases. This aligns with typical performance trends observed with propellers operating in axial flight. In contrast, the edgewise case exhibits a slightly positive trend between the performance coefficients and U_∞/U_{tip}. This indicates favorable performance at lower tip speeds. When comparing C_T and C_Q for varying yaw angles, it is interesting to observe that as the yaw angle increases, the trends for C_Q begin to increase with U_∞/U_{tip}. A slight negative correlation is observed for $\Psi = 70°$, meanwhile C_Q remains relatively constant with for $\Psi = 80°$.

Figure 5.4: Scaled propeller in the edgewise flight configuration ($\Psi = 90°$)

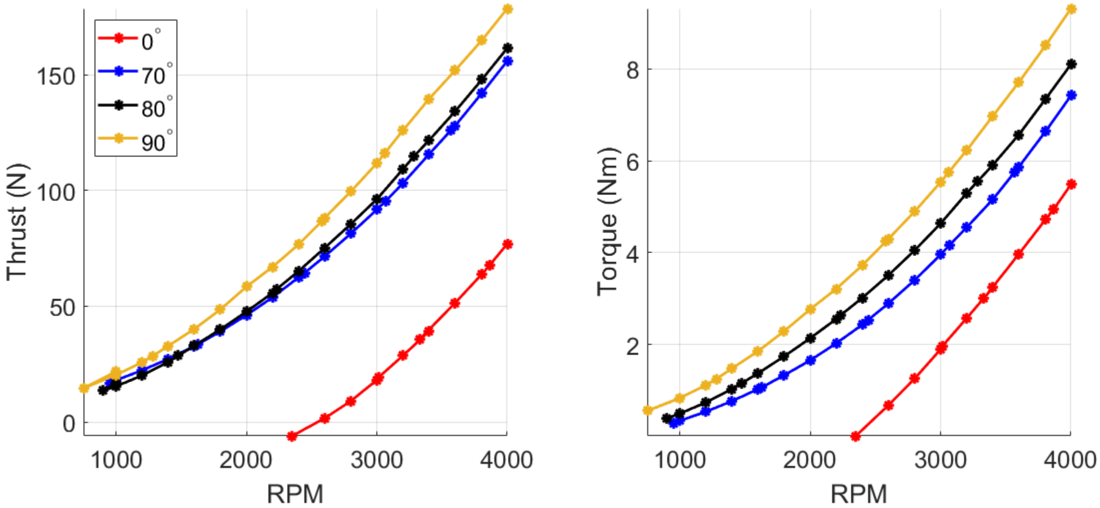

Figure 5.5: Thrust and torque vs RPM measured at varying yaw angles for an inflow velocity of 20 m/s and a pitch angle of 16°

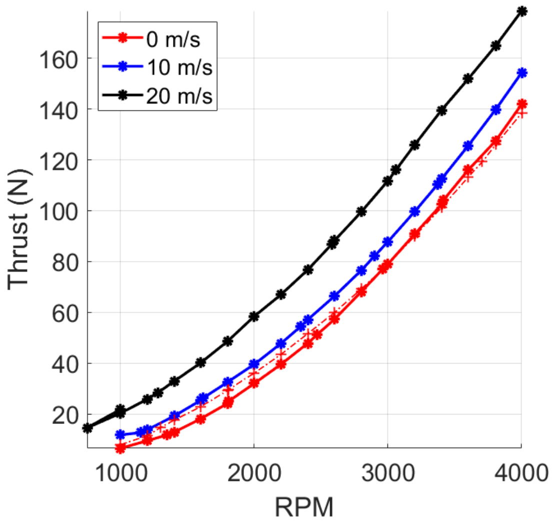

Figure 5.6: Thrust and torque vs RPM measured at varying inflow velocities for a pitch angle of 16° in the edgewise flight condition ($\Psi = 90°$). Dashed lines indicate the 0 m/s case for the axial flight condition.

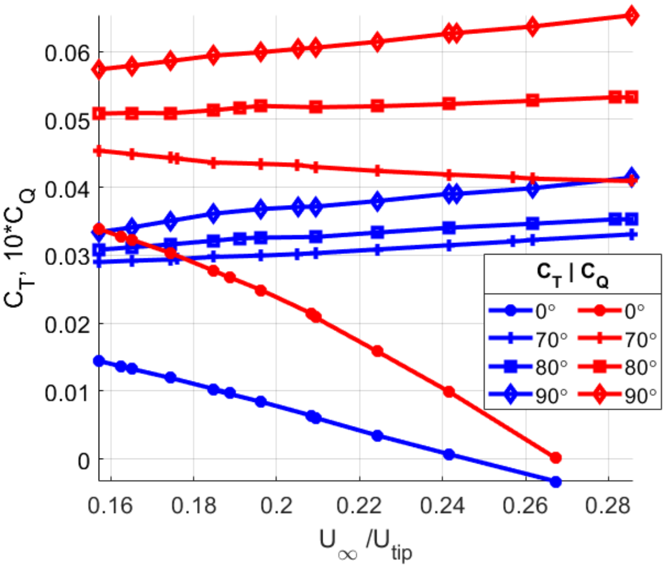

Figure 5.7: Calculated coefficients of thrust (C_T) and torque (C_Q) vs U_∞/U_{tip} for the propeller operating at varying yaw conditions

5.1.3 35% Scale Experiment Comparison

In an investigation by Tinney and Valdez, experimentation was conducted on a 35% geometrically scaled replica of the Joby propeller. Comprised of 5 blades and a diameter of D = 39.96 inches, aerodynamic and acoustic measurements were made for the propeller operating in hover condition for varying pitch angles. Tinney and Valdez present hover performance data for two rotational speeds: 30 rps (rotations per second) and 35 rps, corresponding to $V_{tip} = 95.67$ m/s and $V_{tip} = 111.6$ m/s, respectively. Normalized performance results allow for comparison between experiments at rotation speed with comparable tip speeds for each scaled propeller. Tinney's results are compared to those of the 21% propeller at a blade pitch angle of $\theta = 16°$, with C_T and C_Q values depicted in Figure 5.8. Values for comparison are presented as averages over an RPM range of 3000–3600. This range corresponds to tip speeds comparable to those of the 35% propeller, ranging from 95.76 to 114.9 m/s. Additionally, the results from Tinney and Valdez are interpolated to acquire values of C_T and C_Q for a blade pitch angle of $\theta = 16°$. Comparisons of thrust and power coefficients for these conditions are listed in Table 5.2. This comparison reveals differences of 20.74% and 38.08% in the values of C_T and C_Q, respectively. By using the approximated C_T value for the 35% propeller and applying the properties of the 21% propeller, the scaled thrust is calculated using Equation 2.33 to be approximately 62.51 N. This differs from the experimentally measured thrust of 78.87 N, resulting in a discrepancy of 16.36 N. Based on Tinney's measurements, a blade pitch angle of $\theta = 19.36°$ is estimated to achieve the same C_T as the 21% scale experiment, a difference of 3.36°.

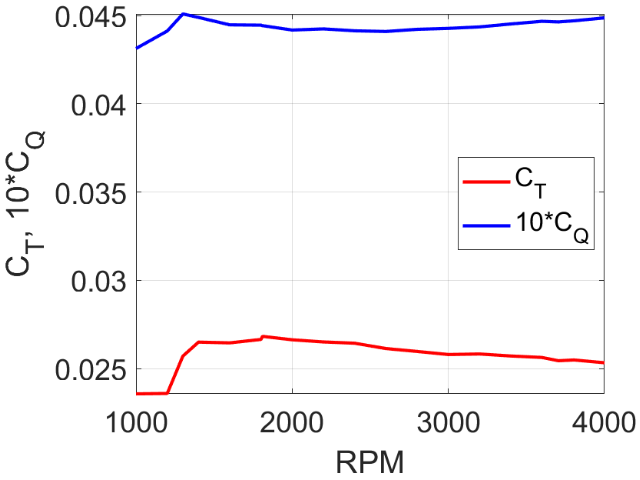

Figure 5.8: Calculated coefficients of thrust (C_T) and torque (C_Q) vs RPM for the 21% scale propeller operating in hover condition

Table 5.2: Comparison of non-dimensionalized performance parameters of the 21% and 35% geometrically scaled eVTOL propellers operating in hover.

Parameter	**21% Scale**	**35% Scale**
C_T	0.0257	0.0204
C_Q	0.00445	0.00275

5.2 BEMT Validation

A BEMT utility was developed to validate the propeller design and enable future aerodynamic predictions. Airfoil sections were generated by taking slices of the CAD geometry of the blade model at 20 radial positions, as seen in Figure 5.9. Slices were taken from r = 2.5” up to 11.78”, corresponding to 0.208-0.98 r/R. The first 15 slices, starting towards the root, are taken at an interval of 0.4643” while the last 5 are taken at an interval of 0.5760”. This allowed for a semi-uniform distribution, with slice #15 coinciding with r/R = 0.75, the reference point for measuring blade pitch. The airfoil slice coordinates were exported from Solidworks into MATLAB, normalized to their chord length, and converted into an XFOIL acceptable format. Lift and drag polars were generated with XFOIL in viscous mode for Reynold’s numbers corresponding to rotational speeds ranging between 100-4000 RPM at intervals of 100. Reynold’s numbers were calculated strictly using the tangential component of velocity. BEMT was implemented in a MATLAB script where the aerodynamic forces of the propeller could be predicted. Values for C_L and C_D were computed by interpolating the lift and drag polars for the angle of attack calculated at each iteration of the BEMT implementation. The relaxation method described by Maheri et al. was additionally applied to improve convergence to a tolerance of 0.1%. An example computation of the aerodynamic loading on a single blade is shown in Figure 5.10. This method was used to compute predictions of thrust and torque for equivalent conditions of the experimental entry and subsequently compared to the measured data from the SWT experiment.

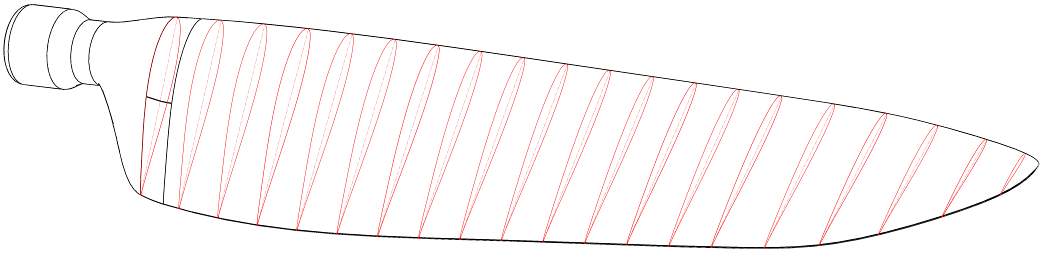

Figure 5.9: Airfoil sections taken at 20 radial positions highlighted in red used for predictive BEMT computations

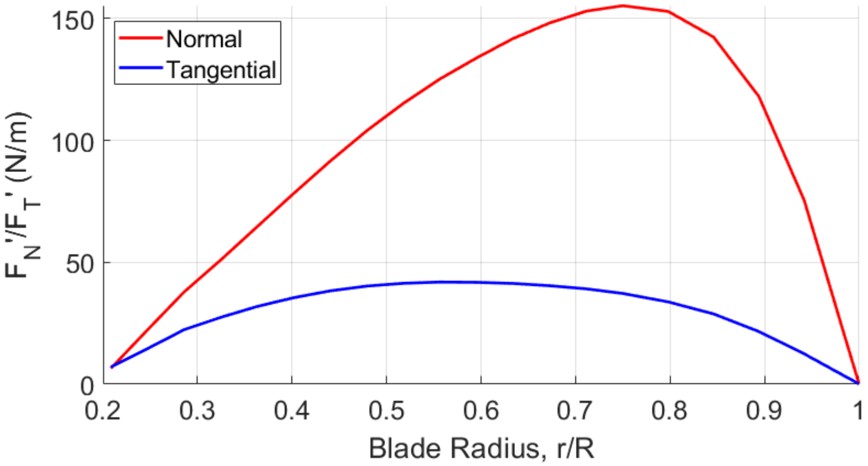

Figure 5.10: Aerodynamic blade loading, normal and tangential force per unit length, computed using BEMT for a single blade at 4000 RPM, 16° pitch, and 10 m/s

5.2.1 Axial Flight

In axial flight, the propeller experiences uniform flow components across the full rotation of azimuth angles, therefore, the blade loading was computed for a single blade, regardless of azimuth angle, and multiplied by the number of blades to predict thrust and torque. Figure 5.11 presents the BEMT results compared with the measured thrust and torque for the axial flight condition at varying inflow speeds. Measured values are presented with uncertainties of ±2.5 N in thrust and ±0.5 Nm in torque to illustrate differences in predictions. The disparity between BEMT predictions and measured results increases with inflow velocity, though predictions generally fall within the measurement uncertainty for the 0 m/s and 10 m/s cases. Comparisons result in maximum values of absolute error for thrust and torque of approximately 13 N and 0.8 Nm, occurring at high operating RPM (Figure 5.12). The relative error is largest at low RPM due to the small values of thrust and torque, however as RPM increases, the relative error for thrust and torque converges below 15%. Greater error is observed at high RPM particularly in the hover case ($U_\infty =$ 0 m/s). This is inferred to be due to the presence of some nonzero inflow during testing at this condition. It was observed that the propeller accelerated the flow which accelerated flow through the test section, resulting in a non-zero inflow velocity. Additionally, BEMT fails with zero inflow velocity, therefore the predictions for hover condition were computed for a freestream velocity of 0.15 m/s. Furthermore, torque is consistently underpredicted, as BEMT only accounts for aerodynamic loading and neglects additional torques such as those from mechanical sources. Strong agreement between the BEMT predictions and measured data in the axial flight condition provides confidence in the propeller design, confirming that it performs predictably as intended.

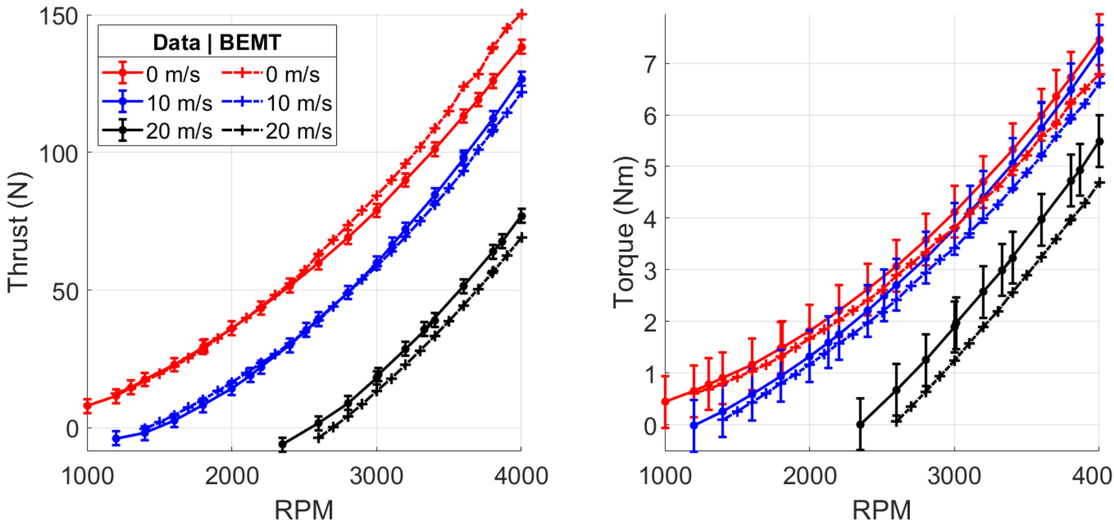

Figure 5.11: Comparison of measured thrust and torque to BEMT predictions at varying inflow velocities for a pitch angle of 16° in the axial flight condition

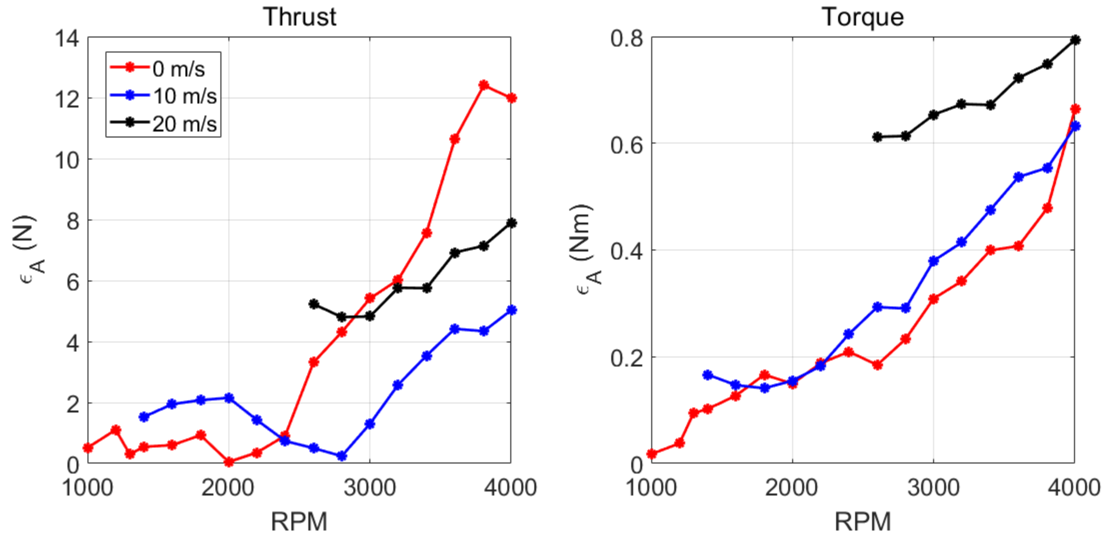

Figure 5.12: Absolute error between measured data and BEMT predictions at varying inflow velocities for a pitch angle of 16° in the axial flight condition

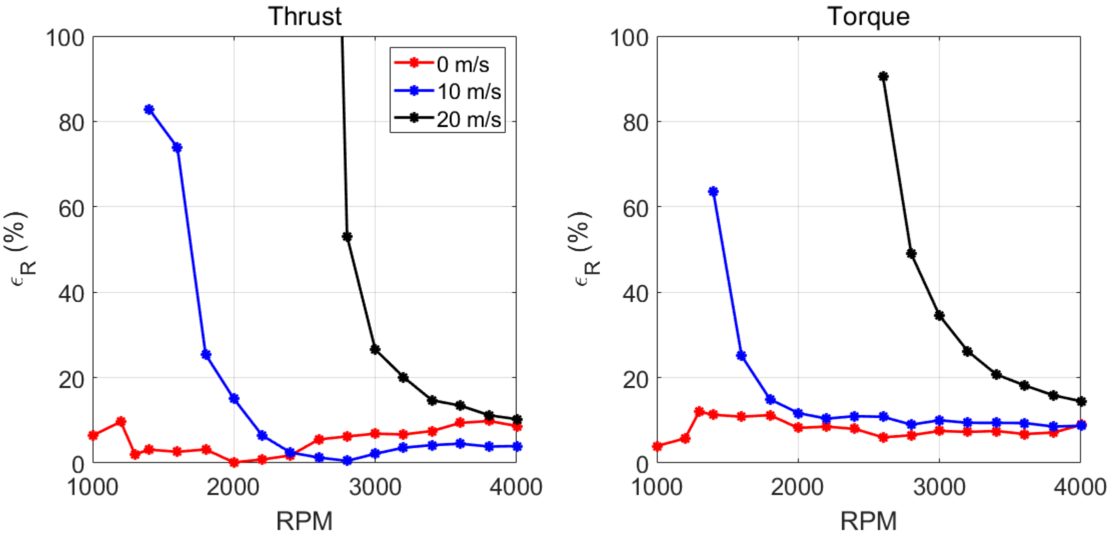

Figure 5.13: Relative error between measured data and BEMT predictions at varying inflow velocities for a pitch angle of 16° in the axial flight condition

5.2.2 Non-Axial Flight

In non-axial flight, the normal component of velocity becomes a function of yaw angle, while the tangential component of velocity becomes a function of yaw angle and blade azimuth. Thus, the normal and tangential velocity equations implemented into the BEMT calculation are modified according to Equation 2.31 and Equation 2.32, respectively. For the edgewise case ($\Psi = 90°$), the normal velocity component is zero. However, BEMT fails at this condition due to a division by zero in Equation 2.17, therefore a velocity of 0.15 m/s is forced in addition to the normal component of velocity to estimate this condition computationally. This addition to the normal component implies a yaw angle of $\Psi = 89.14°$ and $\Psi = 89.57°$ for 10 m/s and 20 m/s, respectively. Due to nonuniform loading across blade azimuth angle, BEMT calculations are performed for azimuth angles from 0° to 360° at 3° increments. The total predicted thrust and torque are calculated as the average of the computed values for a full rotation of azimuth angle. Figure 5.14 depicts the normal and tangential loading, represented as the BEMT result for each blade azimuth angle plotted as a contour. This further highlights the nonuniform loading between the advancing and retreating regions of the propeller. Figure 5.15 compares the measured data to BEMT predictions for varying yaw angles. Both thrust and torque are underpredicted, but the trend with yaw angle remains. The maximum values of absolute error for thrust and torque are approximately 23 N and 2.2 Nm, as seen in Figure 5.17. This result indicates greater discrepancies between BEMT and the measured data in non-axial flight than in axial flight for similar operating conditions. The relative error in thrust is comparatively similar between axial and edgewise flight, however, there is a large increase in relative error for torque, increasing from 14.4% to 23.5%. Additionally, some discrepancies are observed with the predictions made for varying inflow velocities. Illustrated in Figure 5.16, as the inflow velocity increases, the error between BEMT predictions and the measured data increases in edgewise flight. Predictions of thrust fall within the measured uncertainty only at 10 m/s. This remains true for all yaw angles as observed in Figure 5.18 which reveals an increase in relative error between 10 m/s and 20 m/s for each yaw angle across all operating RPM. For 10 m/s inflow velocity, BEMT predictions of thrust and torque converge within 5% and 11% relative error for all yaw angles. Meanwhile, for 20 m/s inflow velocity, predictions of thrust and torque converge within 11% and 23% relative error for all yaw angles. Note that the 0 m/s case for all yaw angles is duplicitous to the hover condition, thus the results are not repeatedly presented. The discrepancies observed in the computational predictions are assumed to be due to BEMT's failure to predict 3D flow effects that are seemingly present in non-axial flight conditions. Overall, the implementation of BEMT for non-axial flight conditions successfully predicted thrust and torque trends, though with larger errors compared to axial flight, particularly at higher inflow velocities.

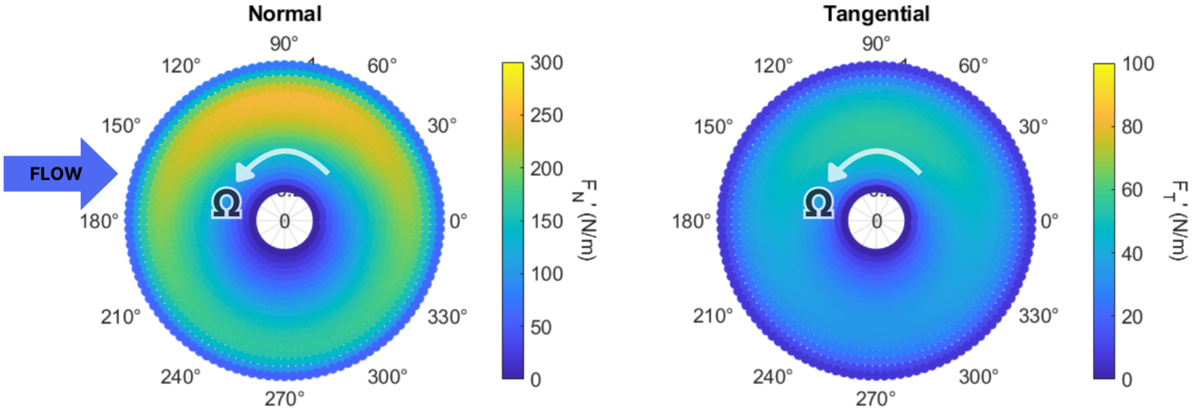

Figure 5.14: Normal (left) and tangential (right) blade loading contours computed using BEMT for $U_\infty = 10$ m/s, $\theta = 16°$, and $\Psi = 90°$ @ 4000 RPM

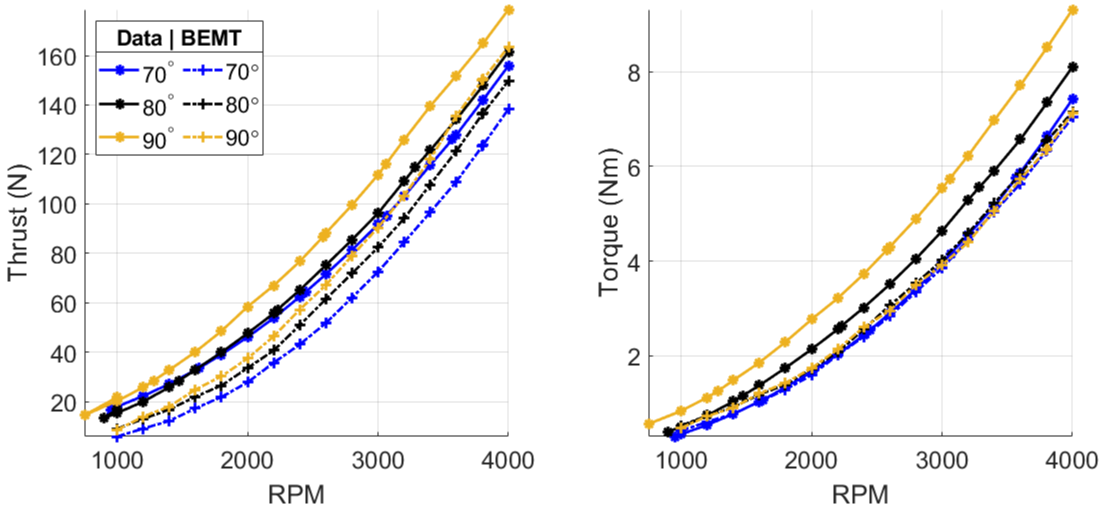

Figure 5.15: Comparison of measured thrust and torque to BEMT predictions at varying yaw angles for an inflow velocity of 20 m/s and a pitch angle of 16°

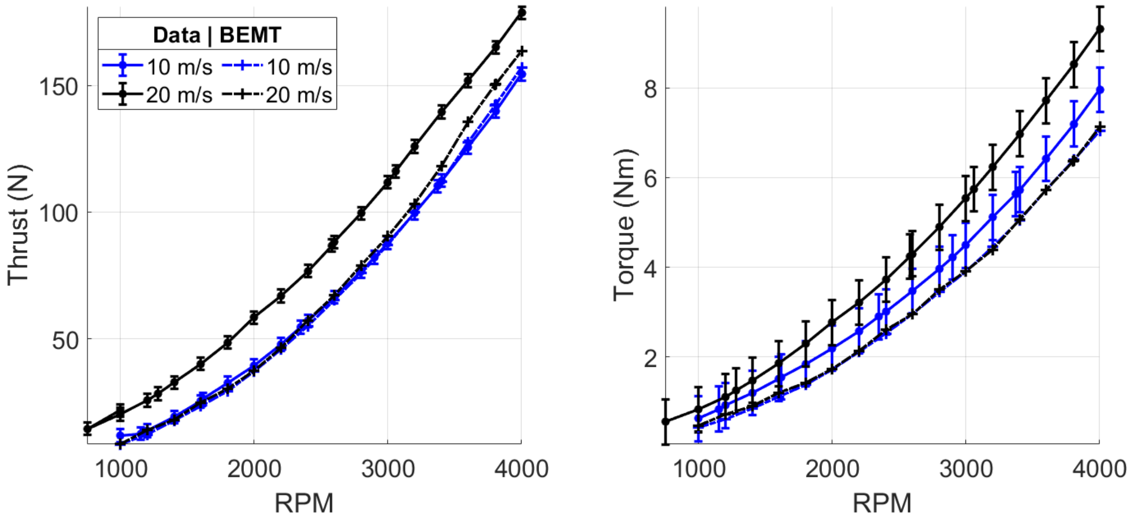

Figure 5.16: Comparison of measured thrust and torque to BEMT predictions at varying inflow velocities for a pitch angle of 16° in the edgewise flight condition ($\Psi = 90°$)

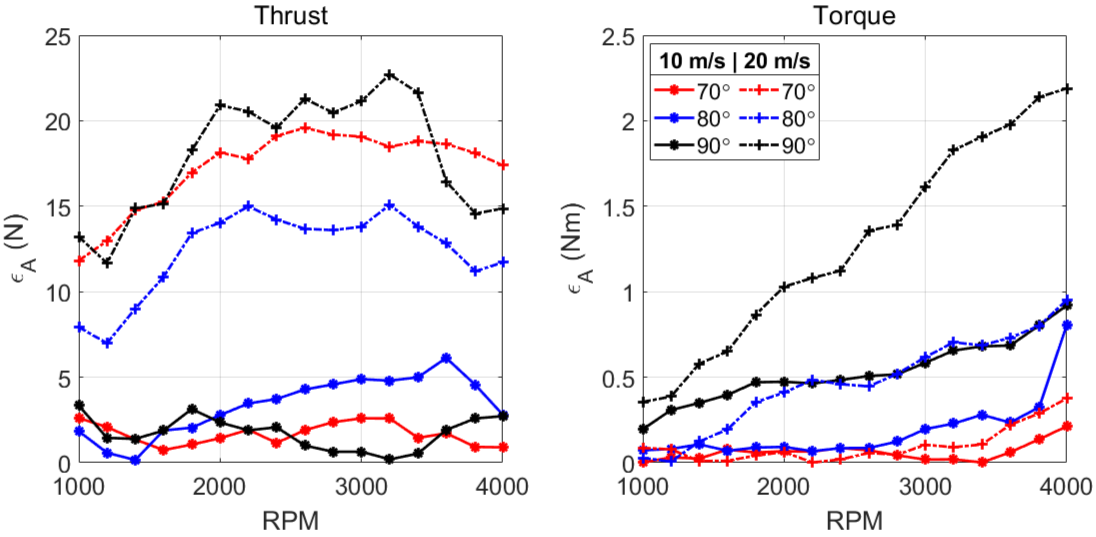

Figure 5.17: Absolute error between measured data and BEMT predictions at varying inflow velocities and yaw for a pitch angle of 16°

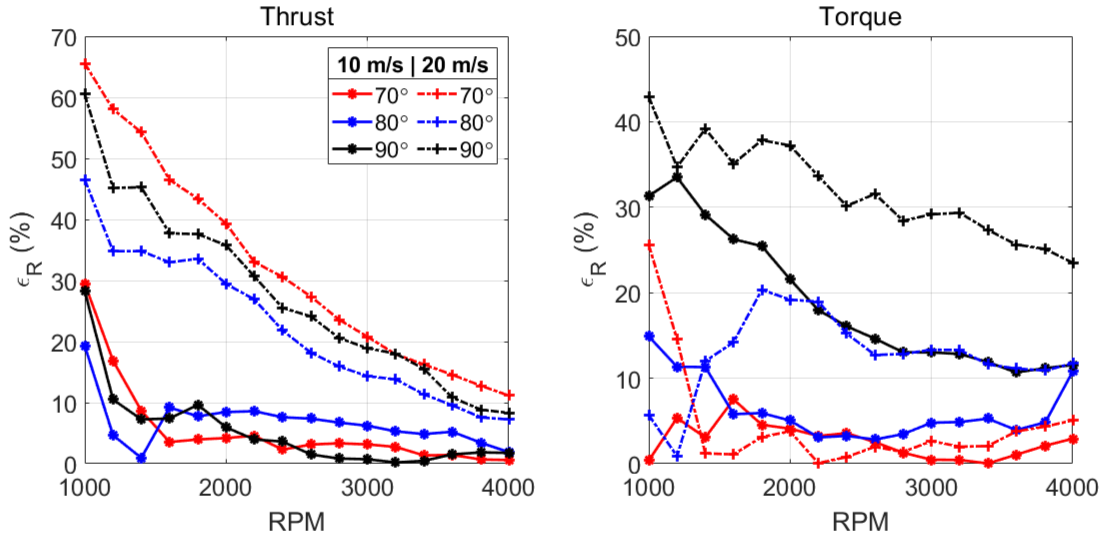

Figure 5.18: Relative error between measured data and BEMT predictions at varying inflow velocities and yaw for a pitch angle of 16°

5.2.3 Inflow Models

The implemented BEMT method considers induced velocity based on the local blade geometry but neglects the variable distribution of the induced velocity field caused by the propeller's wake in non-axial flight. Instead, it assumes a uniform inflow, which fails to accurately represent the non-uniform inflow observed in practice. The induced velocity field is a function of the propeller's generated wake; thus, it is not known prior to experimentation and/or without previous knowledge of the wake profile. Tip vortices produce a highly nonuniform inflow across the propeller disk and implementing complex vortex methods, such as the free-vortex wake model, to model such vortices can be computationally time-consuming. However, the induced velocity field can also be approximated using various low-fidelity inflow models. In the simplest form, a linear inflow model such as the Drees model approximates the inflow distribution as linear. Drees modified an early linear model suggested by Glauert in which the induced inflow is described as a function of weighting factors, representing the deviation of inflow in both the longitudinal and lateral variation. The Drees model allows for the direct calculation of such weights and defines them as functions of wake skew angle and advanced ratio [6]. Furthermore, a more accurate approach called the Mangler & Squire model relates the velocity field to variable pressure loading on the propeller disk. The pressure field is expressed as a linear combination of two loading types: Type-1 (elliptical) and Type-3, which dissipates towards the tips and at the center of the disk [15]. However, implementation requires prior knowledge of the aerodynamic loading.

The inflow variation in the longitudinal and lateral directions across the disk comparing inflow models to experimental results from Elliott et al. are shown in Figure 5.19. These results are for a propeller disk angle of attack of 3°, or similarly defined in the SWT experiment as a yaw angle of 87°. The main discrepancies exist in the leading and trailing edges of the disk and near the propeller hub for the Drees and Mangler & Squire models. It is additionally important to note that Leishman emphasizes that the somewhat large discrepancies between all inflow models and the measured data are thought to be a result of velocity perturbations caused by the propeller hub and fuselage. Moreover, contours of the predicted angle of attack over the propeller disk can be seen in Figure 5.20. The uniform inflow model contour depicts a distribution synonymous with the loading contours predicted using the implemented BEMT method in Figure 5.14. The Mangler & Squire model more evidently depicts greater nonuniformities in the retreating region. Given its complexity, the free-vortex model resolves individual tip vortices in the wake, allowing for the effective capture of nonuniformities in the retreating region while also highlighting the asymmetries between the leading and trailing regions, unlike the other inflow models.

The significant discrepancies between the implemented uniform inflow model and more advanced models indicate that a substantial contribution to the error between the BEMT predictions and experimental measurements can be attributed to the chosen inflow model. The implemented uniform inflow model does not account for the nonuniformities in the induced velocity field, specifically in the retreating and leading edge regions, thus introducing additional errors between the BEMT predictions and measured results. Moreover, the increased discrepancies of the BEMT solutions for higher inflow velocity can be explained by the direct relationship between the induced inflow ratio and the advance ratio [18]. In an effort to reduce the error, it is most desirable to implement the Mangler & Squire model in the future given its more accurate predictions of the induced velocity field and low computational costs. However, this implementation requires pre-existing aerodynamic loading data, which is currently limited. A more feasible alternative would be the application of a linear model, where the induced inflow can be solved analytically. This approach may resolve some of the discrepancies observed with the current BEMT model.

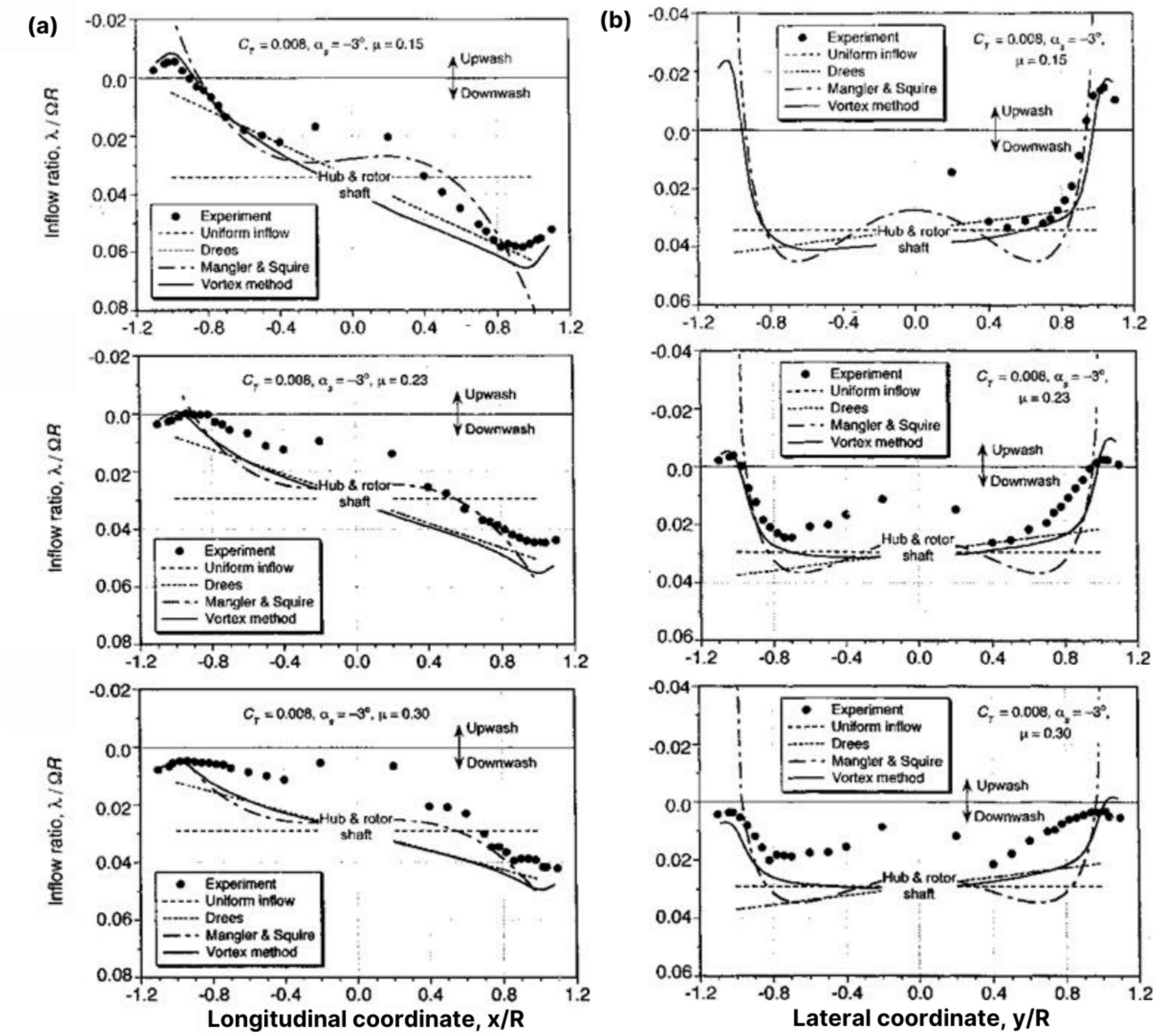

Figure 5.19: Measured variations in the (a) longitudinal and (b) lateral induced inflow across the propeller disk compared to inflow models for various advanced ratios μ. (Adapted from Leishman)

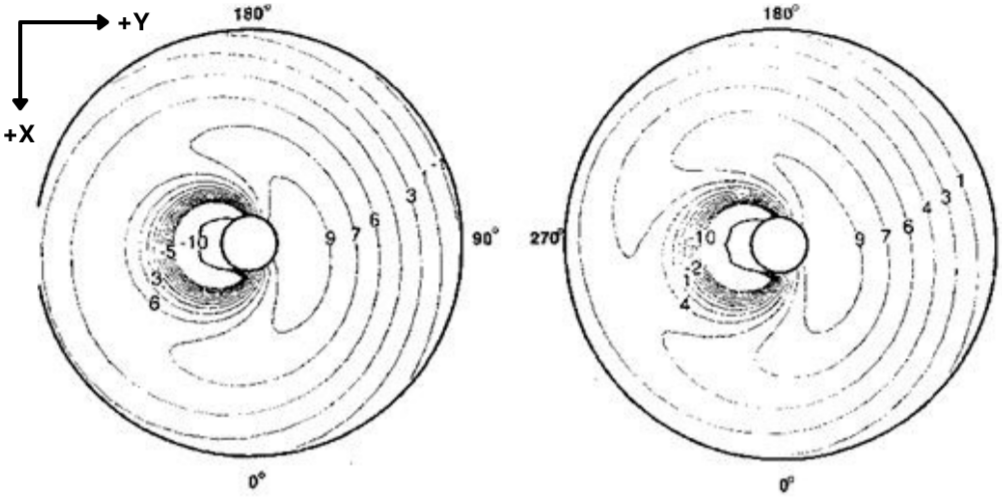

(a) Uniform Inflow Model

(b) Linear Inflow Model

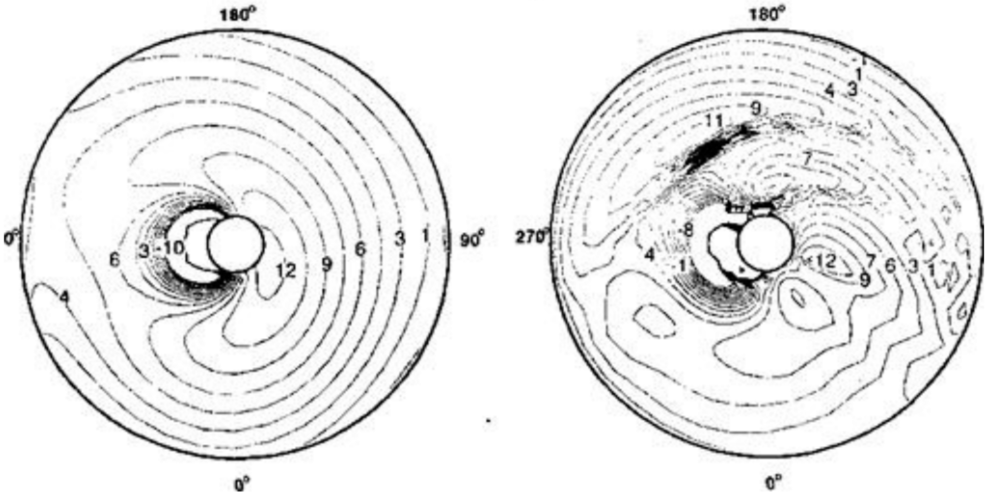

(c) Mangler & Squire Model

(d) Free-Vortex Model

Figure 5.20: Predictions of the angle of attack over the propeller disk for various inflow models. (a) Uniform inflow model. (b) Linear inflow model. (c) Mangler & Squire inflow model. (d) Free-vortex model. (Adapted from Leishman)

5.2.4 Induced Velocity and Distortion

In future experimentation, a deterministic disturbance will be generated and introduced into the flow. This disturbance will convect downstream and interact with the propeller, which is representative of the potential disturbances that may be experienced by a UAM vehicle operating in urban environments. The induced flow generated by the propeller creates a velocity gradient within the propeller plane, causing eddies to undergo stretching and compression. Consequentially, the conservation of angular momentum requires the vorticity of a turbulent eddy to increase/decrease as it compresses/elongates. Although the exact deformation of a turbulent eddy cannot be determined due to limited information about the velocity gradients, the induced velocity components derived from BEMT at the propeller plane can provide valuable insights for making preliminary inferences about the potential distortion of turbulent eddies and the regions of high distortion within the propeller plane.

In Figure 5.21 - Figure 5.24, the lateral (X), vertical (Y), and axial (Z) components of induced velocity are calculated and plotted as contours on the propeller plane for a rotational speed of 4000 RPM and 10 m/s inflow velocity. The propeller in these figures rotates anticlockwise, with the positive Z-axis coming out of the page, in line with the thrust vector, i.e., a negative induced velocity in the Z direction is a net increase in velocity through the propeller plane. These results aim to identify regions of increased induction that may contribute to greater distortion of incoming turbulent flows. While all three components are presented, the lateral and vertical components are of particular interest. The distortion altering the vorticity of eddies aligned in the lateral and vertical directions within the propeller plane induces velocity fluctuations in the velocity component normal to the blades. These fluctuations generate unsteady upwash, leading to unsteady lift and, ultimately, noise generation.

For the axial flight condition, in which the freestream flow vector is in the -Z direction, the magnitude of induced velocity is the lowest of the conditions, with maximum induction of ±4 m/s in the lateral and vertical directions and -11 m/s in the axial direction through the propeller plane. The anticlockwise rotation of the blades produces an antisymmetric distribution of the lateral and vertical components of induced velocity about their respective axes. Additionally, the axial induction is axisymmetric due to the absence of retreating and advancing regions, which may lead to uniform elongation of turbulent eddies across the propeller plane. As the yaw angle increases to 70° and 80°, in which the largest component of the freestream velocity is in the positive X direction, the magnitude of the induced velocity increases in all components. In the yawed cases, the lateral component of the induced velocity loses the symmetry observed in the axial condition, showing a magnitude difference of approximately 2 m/s between the advancing and retreating regions. The advancing region induces flow toward the approximate upstream (-X) direction, while the retreating region induces flow downstream (+X) relative to the yaw angle. Additionally, the vertical component of induced velocity exhibits an antisymmetric distribution about the y-axis, with a maximum magnitude of induction of ±5 m/s. The axially induced velocity exhibits a maximum in the advancing region, with an increase in magnitude of approximately 8.5 m/s relative to the axial flight condition. Lastly, in the edgewise flight condition, where the freestream velocity is in the positive X direction, parallel to the propeller plane, the lateral component of the induced velocity reveals predominant induction in the advancing region, with a maximum magnitude of approximately 7 m/s in the -X direction. The vertical component distribution is similar to that of the other flight conditions, with a distinct region of downward-induced velocity in the upstream region, and upward-induced velocity in the downstream region. The axial component reveals maximum induction in the advancing region, with the largest induction relative to the other flight conditions of -19.5 m/s. In each case, distinct regions of increased induction for the lateral component occur at azimuth angles of $\psi = 90$ and $\psi = 270$, while the lateral component exhibits increased induction at $\psi = 0$ and $\psi = 180$.

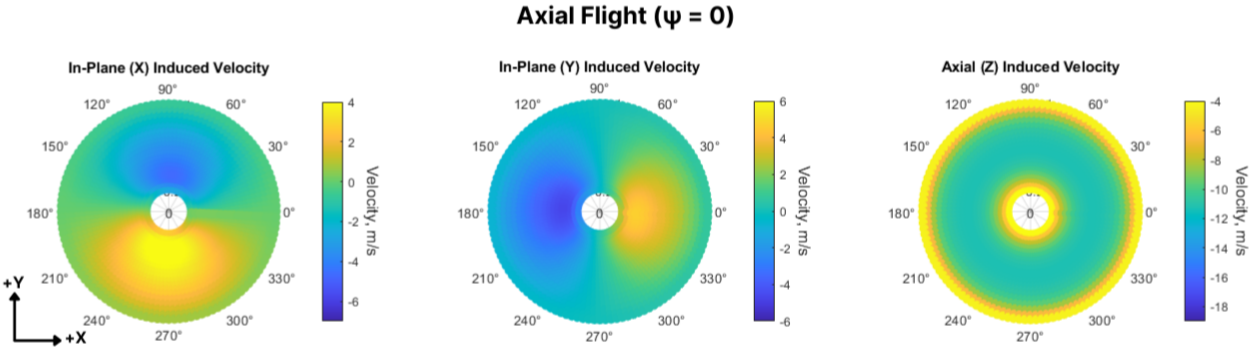

Figure 5.21: BEMT calculations of the lateral, vertical, and axial induced velocity of the propeller operating at 4000 rpm at an inflow velocity of 10 m/s for a blade pitch angle of 16° in the axial flight condition ($\Psi = 0°$)

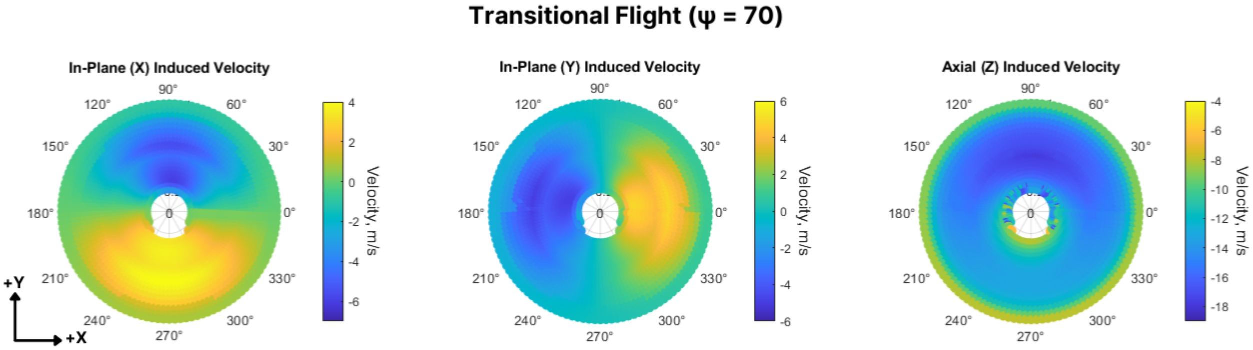

Figure 5.22: BEMT calculations of the lateral, vertical, and axial induced velocity of the propeller operating at 4000 rpm at an inflow velocity of 10 m/s for a blade pitch angle of 16° at a yaw angle of $\Psi = 70°$

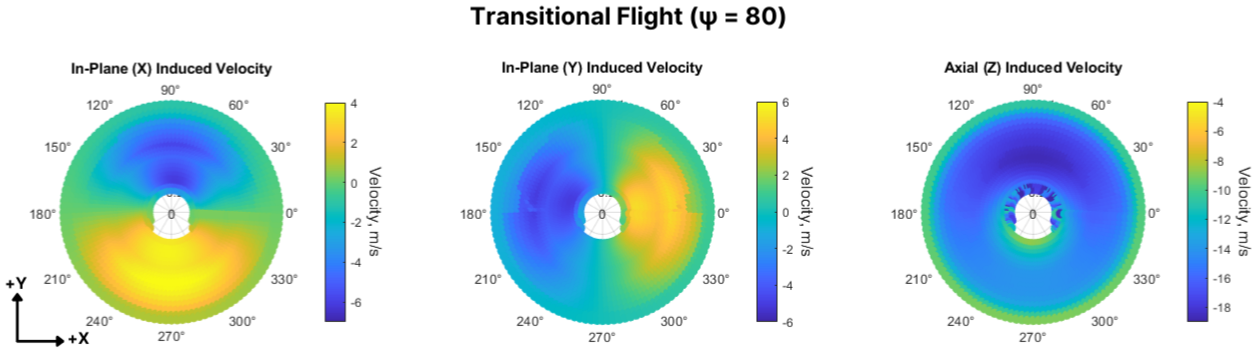

Figure 5.23: BEMT calculations of the lateral, vertical, and axial induced velocity of the propeller operating at 4000 rpm at an inflow velocity of 10 m/s for a blade pitch angle of 16° at a yaw angle of $\Psi = 80°$

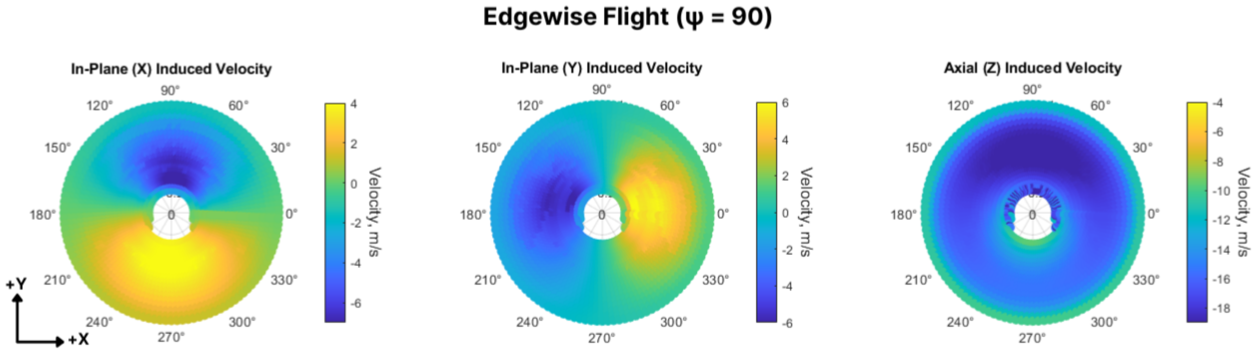

Figure 5.24: BEMT calculations of the lateral, vertical, and axial induced velocity of the propeller operating at 4000 rpm at an inflow velocity of 10 m/s for a blade pitch angle of 16° in the edgewise flight condition ($\Psi = 0°$)

5.3 Acoustic Analysis

In addition to aerodynamic performance, effects on propeller noise are present with changes in flight configuration. Spectra were calculated from the acquired data using Welch's method, applying a Hanning window with 50% overlap and a record length of 8192, resulting in 399 records. The spectra calculated are from pressure time history data acquired by mic #204 (Figure 5.25), corresponding to an observer location at $r_{ob} = 1.62$ m, $\theta_{ob} = 0.196°$, and $\phi_{ob} = -73.3°$. The observer location is in reference to the center of the propeller plane, as defined in Figure 5.26. The noise profile of the propeller is predominantly broadband due to propeller self-noise. Additionally, the tones present at low frequencies are artifacts of the BPF and multiples of the BPF. Acoustic spectra are compared for varying flight conditions across a frequency range of 200-25000 Hz, with the minimum being the anechoic limit of the test section. Spectra for a rotational speed of $\Omega = 4000$ RPM are computed, resulting in a BPF = 333 Hz. The following sections analyze the effects of flight conditions on the noise profile of the propeller in both axial and non-axial flight.

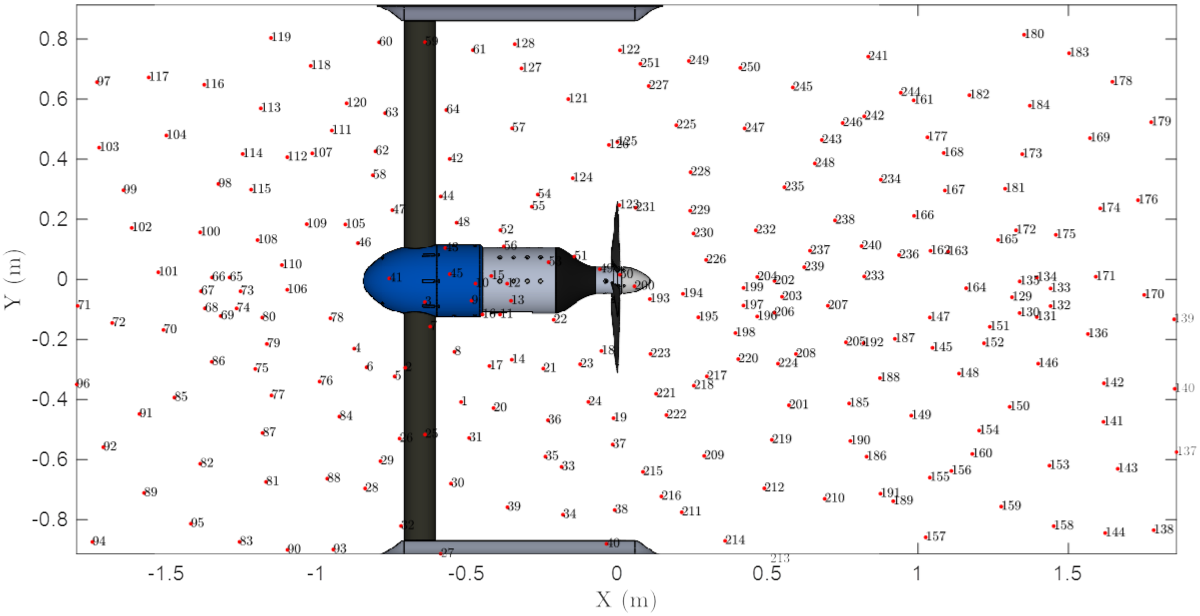

Figure 5.25: Map of the microphone locations relative to the propeller

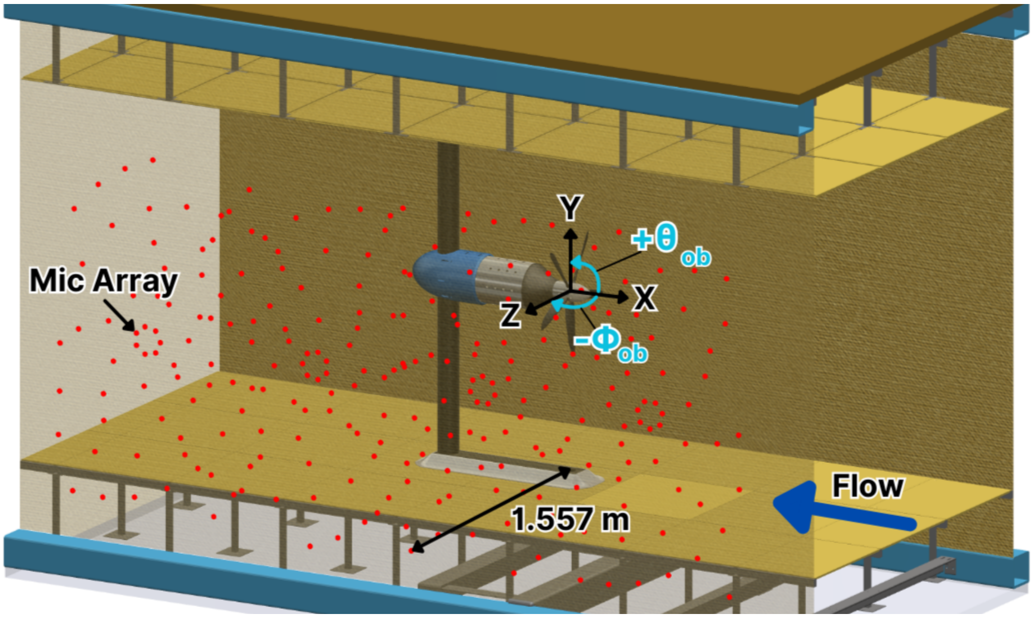

Figure 5.26: Coordinate frame defining the observer location

5.3.1 Axial Flight

The computed spectra are shown in Figure 5.27 for varying inflow velocities in axial flight. From this, it is evident that a greater inflow velocity correlates to increased acoustic power. It is observed that the spectra collapse between 1-10 kHz with multiples of the BPF visible at ~200, 269, and 331 Hz for each inflow condition operating at 4000 RPM. However, it is suspected that the majority of acoustic power is due to mechanical and background noise sources. The dotted lines in Figure 5.27 depict the background noise measurements made for each respective inflow velocity, with the propeller removed from the shaft assembly and the motor enabled. These measurements do not indicate the contribution of mechanical noise to the overall acoustic intensity. However, further analysis of the noise sources in axial flight by the beamform maps illustrated in Figure 5.28 suggests mechanical sources are a significant noise source. The resultant beamform map at 2000 Hz indicates that the dominant sources can be attributed to motor noise, mechanical vibrations in the shaft, and potential contributions from the mounting structure. At a higher frequency of 8000 Hz, the propeller accounts for a negligible portion of the overall noise profile. Figure 5.29 illustrates a map of the sound pressure level (SPL) level computed for the broadband (400-20000 Hz), excluding the tones at the BPF multiples, at 4000 rpm and 20 m/s for every microphone. The largest SPL measured is ~73.5 dB occurring downstream of the propeller plane. The relatively quiet profile of the propeller is suspected to be due to the blade geometry, in which the majority of the normal component of loading is shifted away from the tip, occurring predominantly between 60%-85% blade radius, as predicted by BEMT (Figure 5.10) in Section 5.2.

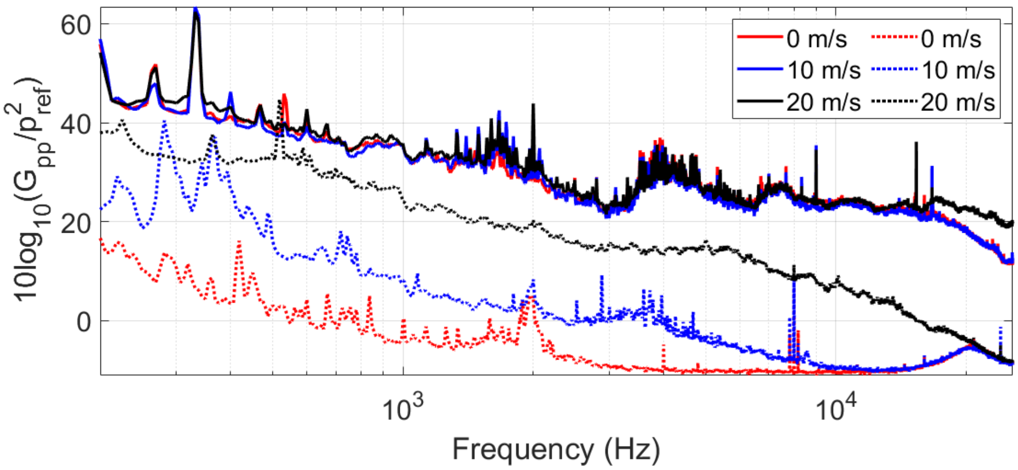

Figure 5.27: Calculated autospectra at 4000 rpm operating at varying inflow velocities for a pitch angle of 16° in the axial flight condition ($\Psi = 0°$). Dotted lines indicate background noise measurements for the respective inflow velocity.

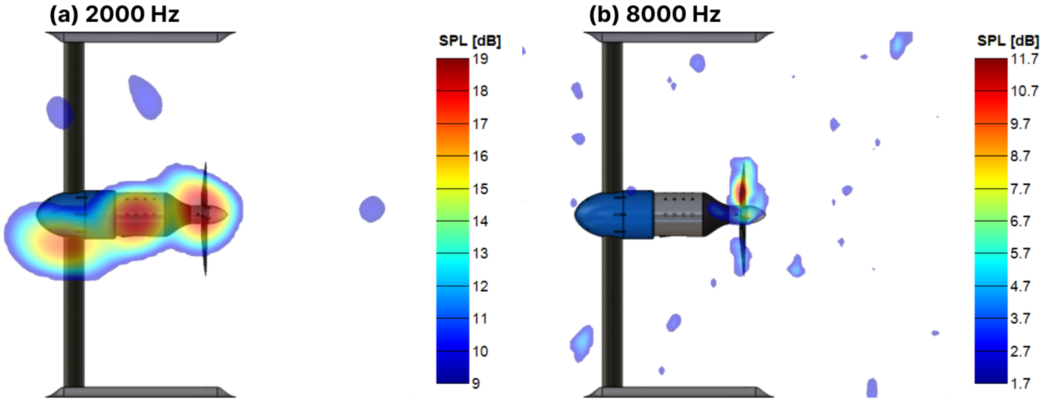

Figure 5.28: Beamform maps for (a) 2000 Hz and (b) 8000 Hz showing acoustic source location operating at 4000 rpm and 20 m/s for a pitch angle of 16° in the axial flight condition ($\Psi = 0°$)

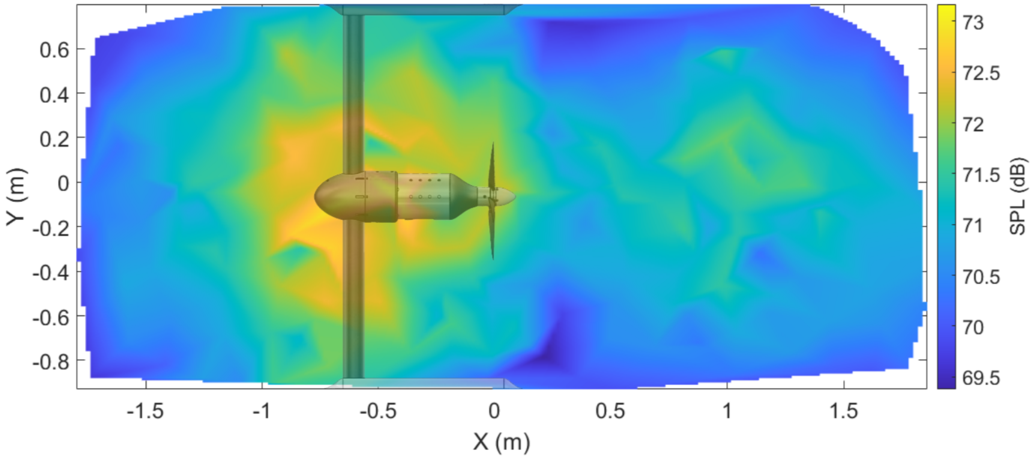

Figure 5.29: SPL contour map (400-20000 Hz) at 4000 rpm and 20 m/s for a pitch angle of 16° in the axial flight condition ($\Psi = 0°$)

5.3.2 Non-Axial Flight

The computed spectra are shown in Figure 5.31 for varying inflow velocities in edgewise flight. Similar to axial flight, a greater inflow velocity correlates to increased acoustic power. However, in contrast to axial, this increase is present across all frequencies, unlike the collapse observed in axial flight. In addition, the acoustic power is distributed over a larger range of frequencies, up to ∼4000 Hz, before dropping off. For the 0 m/s case, haystacking is evident, with additional tones peaking at integer multiples of the BPF. This is believed to result from the recirculation of flow ingested by the propeller, driven by its proximity to the test section wall in the edgewise configuration, i.e., $\Psi = 90°$. This phenomenon diminishes with the introduction of inflow, as the propeller wake is convected downstream, thereby reducing the effects of recirculation. This result shares similarities with the findings reported by Tinney and Valdez for a 35% scaled Joby propeller operating in hover at 30 rps ($V_{tip} = 95.66$), in which the BPF and its harmonics dominate the acoustic profile in hover condition. Figure 5.31 highlights this similarity, showing the presence of haystacked tones at multiples of the BPF—a feature that is notably absent in the spectra of the axial hover configuration, as previously discussed in Section 5.3.1.

Figure 5.30 depicts an increasing correlation between acoustic power and operating RPM. This clearly demonstrates the positive relationship between noise and blade loading, given that thrust and torque also increase with RPM as discussed in Section 5.1. When comparing the noise at varying yaw, as shown in Figure 5.32, it is evident that the acoustic power increases with the yaw angle. In the non-axial cases, a significant increase in acoustic power was observed in the mid-frequency range, which is absent in axial flight. This is presumed to result from an increase in unsteady loading during non-axial flight, possibly caused by blade-wake interaction. This results in an approximate SPL increase of 30 dB between the axial and non-axial flight conditions. It is important to emphasize that, although the change in mean loading between the non-axial conditions is minimal, the greater variation in acoustic intensities can be attributed to unsteady loading, which is not captured in the mean loading measurements presented in Section 5.1. The increase in propeller noise can additionally be observed in the beanform maps illustrated in Figure 5.33, for the identical conditions previously computed for the axial flight condition. Contrasting the axial flight condition, these results indicate that the propeller is the dominant source of noise at both low and mid frequencies, with minimal contribution from mechanical sources to the overall sound pressure level. Furthermore, at 8000 Hz, the blades are clearly identified as the primary noise source, exhibiting an SPL increase of approximately 55 dB relative to axial flight. Lastly, the SPL map illustrated in Figure 5.34 reveals an increase in SPL of ∼5 dB in the upstream region of the propeller as compared to the downstream region.

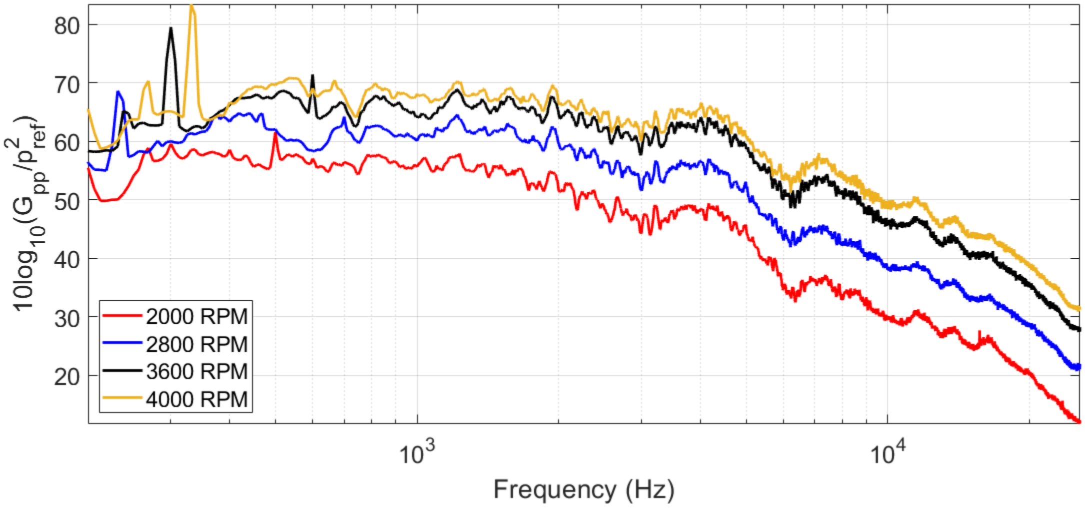

Figure 5.30: Calculated autospectra for varying RPM at 20 m/s inflow velocity and a pitch angle of 16° in the edgewise flight condition ($\Psi = 90°$)

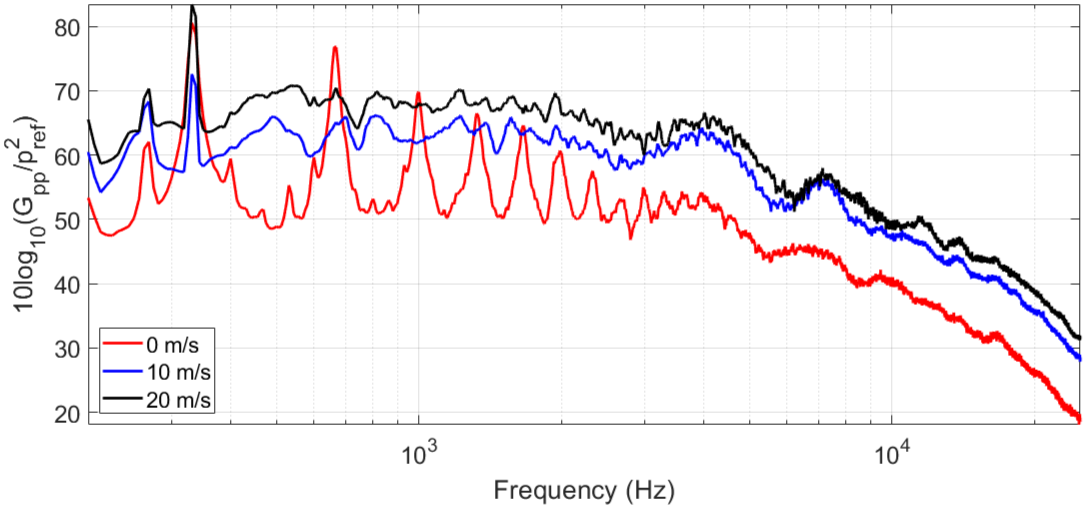

Figure 5.31: Calculated autospectra at 4000 rpm operating at varying inflow velocities for a pitch angle of 16° in the edgewise flight condition ($\Psi = 90°$)

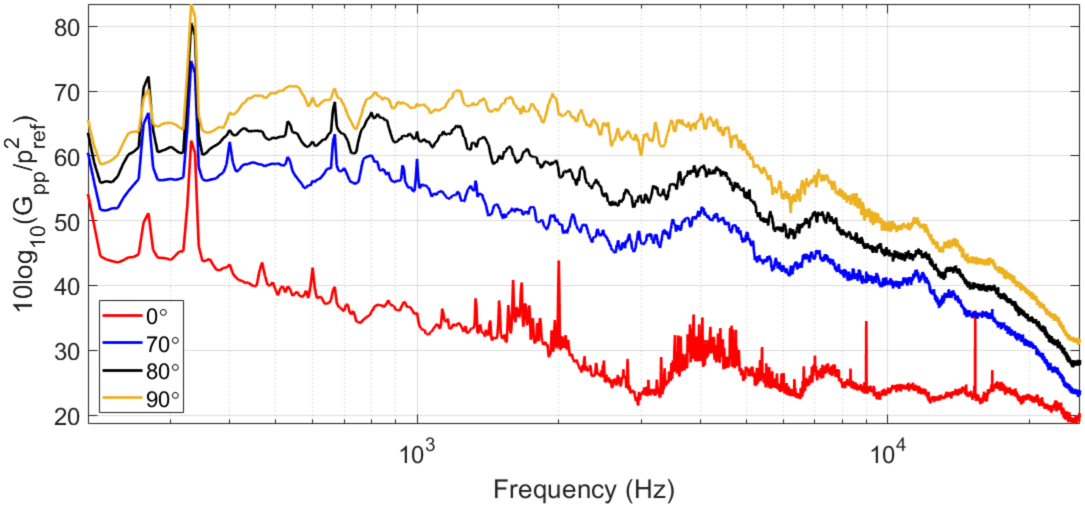

Figure 5.32: Calculated autospectra at 4000 rpm operating at varying yaw angles for an inflow velocity of 20 m/s and pitch angle of 16°

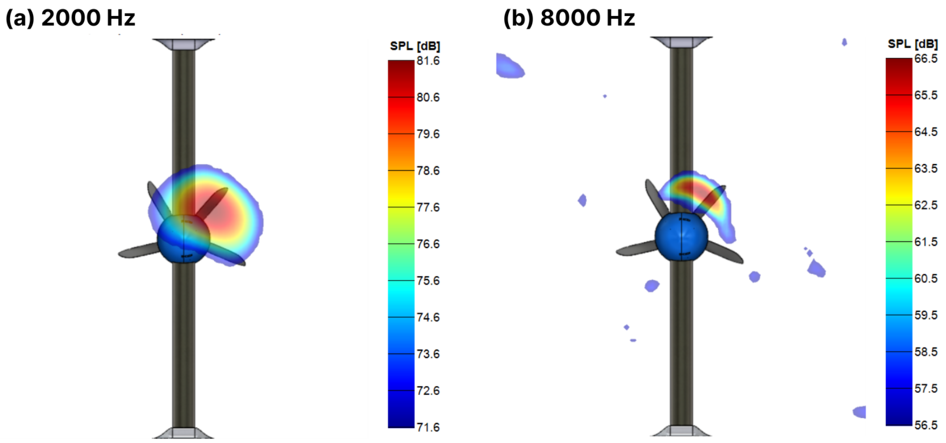

Figure 5.33: Beamform maps for (a) 2000 Hz and (b) 8000 Hz showing acoustic source location operating at 4000 rpm and 20 m/s for a pitch angle of 16° in the edgewise flight condition ($\Psi = 90°$)

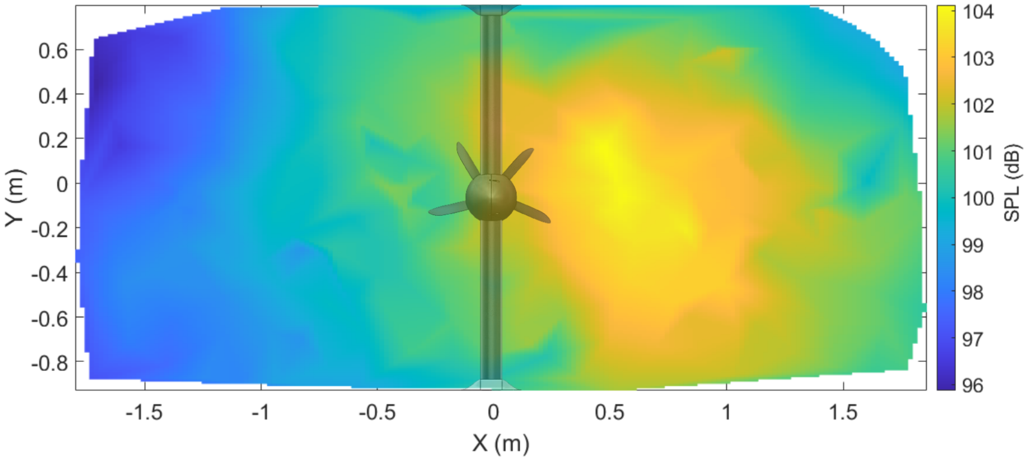

Figure 5.34: SPL contour map (400-20000 Hz) at 4000 rpm and 20 m/s for a pitch angle of 16° in the edgewise flight condition ($\Psi = 90°$)

Chapter 6

Summary and Conclusions

A scaled version of the 2017 Joby eVTOL propeller was designed for wind tunnel experimentation to collect aerodynamic and acoustic performance data in both axial and edgewise flight, in an effort to support CFD validation. Designed with adjustable pitch and yaw capabilities, the scaled propeller was tested in the Virginia Tech Stability Wind Tunnel, operating through a sweep of RPM in flow speeds ranging from 0 to 20 m/s. Thrust, torque, and sound pressure measurements were acquired for each condition. In addition to the experimentation, a predictive utility was developed using Blade Element Momentum Theory to estimate thrust and torque values for the corresponding experimental conditions. Predictions were subsequently compared to measured data to validate its predictive capabilities. The results of this study are summarized as follows:

In axial flight:

- Thrust and torque increase proportionally to the square of the rotation speed.
- Thrust and torque decrease as the inflow velocity increases.
- Thrust and torque increase as the blade pitch angle increases.
- BEMT predictions of thrust and torque converge below 10% relative error for low inflow velocities and increase to 15% for 20 m/s inflow.
- Noise profile is predominantly tonal noise associated with the blade passage frequency, mechanical noise, and background noise. Beamforming maps support assumptions of the noise sources.

In non-axial flight:

- Thrust and torque increase as the yaw angle increases.
- Thrust and torque increase as the inflow velocity increases.
- For 10 m/s inflow velocity, BEMT predictions of thrust and torque converge within 5% and 11% relative error for all nonzero yaw angles. Meanwhile, for 20 m/s inflow velocity, the relative error in the predictions of thrust and torque increases to 11% and 23% for all nonzero yaw angles.

- Large errors in the predicted thrust and torque, particularly at high inflow velocities, are believed to be primarily due to the implemented uniform inflow model which fails to account for nonuniformities consequential of edgewise flight.
- Supplemental BEMT calculations provide insights into regions of increased velocity induction as a preliminary study of the propeller's interactions with turbulence flows.
- The noise profile includes tonal noise associated with the blade passage frequency, along with a significant increase in broadband noise compared to axial flight. This is suspected to be caused by blade-wake interaction.
- Overall acoustic intensity increases with RPM, inflow velocity, and yaw angle.
- The sound pressure level in edgewise flight increased ~ 30 dB in comparison to axial flight.

Bibliography

[1] Akinlabi, E., Maronga, B., Giometto, M. G., and Li, D. (2022). Dispersive fluxes within and over a real urban canopy: A large-eddy simulation study. *Boundary-Layer Meteorology*, 185:93–128.

[2] Alexander, W. N. and Hickling, C. (2017). Analysis of low-frequency acoustic sources in the virginia tech stability wind tunnel. In *ASME International Mechanical Engineering Congress and Exposition*, volume 13: Acoustics, Vibration and Phononics.

[3] Bacchini, A. and Cestino, E. (2019). Electric vtol configurations comparison. *Aerospace*, 6(3):26.

[4] Brooks, T. F., Pope, D. S., and Marcolini, M. A. (1989). Airfoil self-noise and prediction. Technical Report L-16528, NASA.

[5] Brown, K., Devenport, W., and Borgoltz, A. (2019). Exploitation of hybrid anechoic wind tunnels for aeroacoustic and aerodynamic measurements. *CEAS Aeronautical Journal*, 10:251–266.

[6] Chen, R. T. (1989). A survey of nonuniform inflow models for rotorcraft flight dynamics and control applications. Technical Report A-89220, NASA.

[7] Droandi, G. and Gibertini, G. (2015). Aerodynamic shape optimisation of a proprotor and its validation by means of cfd and experiments. *The Aeronautical Journal*, 119(1220):1223–1251.

[8] Elliott, J. W., Althoff, S. L., and Sailey, R. H. (1988). Inflow measurements made with a laser velocimeter on a helicopter model in forward flight, volume 1, rectangular planform blades at an advance ratio of 0.15. Technical Report TM-100541, NASA.

[9] Glauert, H. (1983). *The Elements of Aerofoil and Airscrew Theory.* Cambridge University Press.

[10] Gur, O. and Rosen, A. (2008). Multidisciplinary design optimization of a quiet propeller. In *14th AIAA/CEAS Aeroacoustics Conference (29th AIAA Aeroacoustics Conference).*

[11] Hanson, L., Yi, Z., Zang, B., and Azarpeyvand, M. (2025). Rotor noise in non-axial inflow conditions. *Applied Acoustics*, 228.

[12] Kurtz, D. W. and Marte, J. E. (1970). A review of aerodynamic noise from propellers, rofors, and liff fans. Technical Report 32-1462, Jet Propulsion Laboratory, California Institute of Technology.

[13] Lam, W., Hamil, G., Song, Y., Robinson, D., and Raghunathan, S. (2011). A review of the equations used to predict the velocity distribution within a ship's propeller jet. *Ocean Engineering*, 38(1):1–10.

[14] Ledoux, J., Riffo, S., and Salomon, J. (2021). Analysis of the blade element momentum theory. *SIAM Journal on Applied Mathematics*, 81(6):2596–2621.

[15] Leishman, G. J. (2006). *Principles of helicopter aerodynamics with CD extra*. Cambridge University Press.

[16] Maheri, A., Noroozi, S., Toomer, C., and Vinney, J. (2006). Damping the fluctuating behaviour and improving the convergence rate of the axial induction factor in the bemt-based rotor aerodynamic codes. In *European Wind Energy Conference & Exhibition*, volume 2, pages 1176–1179.

[17] McCrink, M. H. and Gregory, J. W. (2017). Blade element momentum modeling of low-reynolds electric propulsion systems. *Journal of Aircraft*, 54(1):163–176.

[18] Niemiec, R. and Gandhi, F. (2016). Effects of inflow model on simulated aeromechanics of a quadrotor helicopter. In *72nd Annual Forum of the American Helicopter Society International*.

[19] Pascioni, K. A., Watts, M. E., Houston, M., Lind, A., Stephenson, J. H., and Bain, J. (2022). Acoustic flight test of the joby aviation advanced air mobility prototype vehicle. In *28th AIAA/CEAS Aeroacoustics 2022 Conference*.

[20] Radotich, M. (2022). Conceptual design of tiltrotor aircraft for urban air mobility. In *Aeromechanics for Advanced Vertical Flight Technical Meeting, Transformative Vertical Flight 2022*.

[21] Rankine, W. J. M. (1865). On the mechanical principles of the action of propellers. *Transactions of the Institution of Naval Architects*, 6.

[22] Remillieux, M., Crede, E., Camargo, H., Burdisso, R., Devenport, W., Rasnick, M., Van Seeters, P., and Chou, A. (2008). Calibration and demonstration of the new virginia tech anechoic wind tunnel. In *14th AIAA/CEAS Aeroacoustics Conference (29th AIAA Aeroacoustics Conference)*.

[23] Rizzi, S., Huff, D., Boyd Jr., D. D., Bent, P., Henderson, B., Pascioni, K., Sargent, D. C., Josephson, D., Marsan, M., He, H., and Snider, R. (2020). Urban air mobility noise: Current practice, gaps, and recommendations. Technical Report TP-20205007433, NASA.

[24] Shahjahan, S., Gong, A., Moore, A., and Verstraete, D. (2024). Optimisation of proprotors for tilt-wing evtol aircraft. *Aerospace Science and Technology*, 144.

[25] Sørensen, J. N. (2016). *General momentum theory for horizontal axis wind turbines*, volume 4. Springer.

[26] Thai, A., Bain, J., Mikic, G., and Stoll, A. (2023). Flyover noise computations of the joby aviation aircraft. In *Vertical Flight Society 79th Annual Forum*.

[27] Thurman, C. S. and Baeder, J. D. (2023). Blade-wake interaction noise for small hovering rotors, part 1: Characterization study. *AIAA Journal*, 61(6):2552–2569.

[28] Tinney, C. E. and Valdez, J. A. (2024). Hover performance and acoustics of a 35% scale notional evtol rotor. In *30th AIAA/CEAS Aeroacoustics Conference (2024)*.

[29] Zhang, T., Barakos, G., and Furqan (2024). On the aerodynamic performance of redundant propellers for multi-rotor evtol in cruise. *Aerospace Science and Technology*, 145.